photonics

MDPI

Review

Harnessing Ultra-Intense Long-Wave Infrared Lasers: New Frontiers in Fundamental and Applied Research

Igor V. Pogorelsky * and Mikhail N. Polyanskiy

Brookhaven National Laboratory, Upton, NY 11973, USA; polyanskiy@bnl.gov
* Correspondence: igor@bnl.gov; Tel.: +1-631-344-5801

Abstract: This review explores two main topics: the state-of-the-art and emerging capabilities of high-peak-power, ultrafast (picosecond and femtosecond) long-wave infrared (LWIR) laser technology based on CO_2 gas laser amplifiers, and the current and advanced scientific applications of this laser class. The discussion is grounded in expertise gained at the Accelerator Test Facility (ATF) of Brookhaven National Laboratory (BNL), a leading center for ultrafast, high-power CO_2 laser development and a National User Facility with a strong track record in high-intensity physics experiments. We begin by reviewing the status of 9–10 μm CO_2 laser technology and its applications, before exploring potential breakthroughs, including the realization of 100 terawatt femtosecond pulses. These advancements will drive ongoing research in electron and ion acceleration in plasma, along with applications in secondary radiation sources and atmospheric energy transport. Throughout the review, we highlight how wavelength scaling of physical effects enhances the capabilities of ultra-intense lasers in the LWIR spectrum, expanding the frontiers of both fundamental and applied science.

Keywords: ultra-high intensity lasers; long-wave infrared; chirped pulse amplification; nonlinear pulse compression; laser interaction with matter; laser plasma electron acceleration; laser plasma ion acceleration; inverse Compton scattering; future collider; directed energy

Received: 14 January 2025
Revised: 19 February 2025
Accepted: 26 February 2025
Published: 28 February 2025

Citation: Pogorelsky, I.V.; Polyanskiy, M.N. Harnessing Ultra-Intense Long-Wave Infrared Lasers: New Frontiers in Fundamental and Applied Research. *Photonics* **2025**, *12*, 221. https://doi.org/10.3390/photonics12030221

1. Introduction

High-peak-power lasers operating in the 0.8–1.2 μm wavelength range have been instrumental in advancing experimental strong-field physics. Extending their spectral range from the near-infrared (NIR) into the long-wave infrared (LWIR) domain (8–14 μm) unlocks new possibilities for optimizing established laser-matter interaction regimes and exploring novel mechanisms. This spectral expansion enhances critical physical processes with far-reaching implications, driving advancements in high-profile applications such as particle acceleration, secondary radiation sources, and long-distance atmospheric laser beam transport—all benefiting from the wavelength-dependent scaling of these interactions.

Recent advancements in high-peak-power LWIR laser technology have been propelled by the development of multi-terawatt, picosecond systems, such as those at UCLA [1] and the Brookhaven National Laboratory (BNL) Accelerator Test Facility (ATF) [2,3].

This paper reviews the capabilities of the BNL ATF picosecond LWIR laser, explores opportunities for its advancement toward the multi-terawatt femtosecond regime, and examines its current and emerging research applications. The focus on ATF is justified by its status as one of the leaders in advanced LWIR laser development and its role as a National User Facility with the most extensive record of multidisciplinary experiments in the LWIR spectral domain.

Section 2 provides an overview of state-of-the-art high-power LWIR laser technology based on gas-discharge CO_2 laser amplifiers, highlighting the ATF laser system as a leading example.

- Section 2.1 provides a brief history of high-peak-power LWIR lasers. The state-of-the-art is exemplified by the BNL system, which utilizes chirped pulse amplification (CPA) [4] and a multi-isotope, high-pressure CO_2 gas laser medium operating at λ = 9.2 µm [2]. The combination of these innovations, unprecedented for CO_2 lasers, marks a significant milestone in advancing LWIR laser technology, addressing the stringent demands of modern ultra-high-peak-power systems.
- Section 2.2 outlines ongoing research and development efforts aimed at advancing ultra-intense LWIR lasers into the sub-picosecond time domain—potentially down to a few optical cycles—and achieving ~100 TW peak intensity in a single beam.
- Section 2.3 addresses the potential for developing high-repetition-rate, terawatt-class LWIR lasers with kilowatt-level average power and briefly discusses the possibilities for compact, mobile, short-pulse, optically pumped CO_2 lasers.

Section 3 focuses on examining the benefits of wavelength scaling in physical processes critical to laser plasma acceleration of electrons and ions.

- Section 3.1 compiles topics on wavelength scaling in fundamental laser-matter interaction processes, including ionization, laser propagation in plasma up to critical plasma density and the relativistic self-focusing regime, ponderomotive electron motion, and generation of plasma waves.
- Section 3.2 delves into laser wakefield electron acceleration (LWFA), focusing on how long-wavelength lasers facilitate the formation of large-scale plasma bubbles in low-density plasmas. The unique capabilities of the ATF—integrating the LWIR laser with NIR lasers and an RF electron linear accelerator (linac)—support trailblazing research aimed at addressing key challenges in exploring and improving the performance of laser–plasma accelerators. These efforts have far-reaching implications, including the ambitious goal of developing a TeV-class electron–positron (e^-e^+) collider, a transformative breakthrough with the potential to redefine the frontiers of particle physics.
- Section 3.3 explores laser-driven ion acceleration, highlighting how the $\propto \lambda^{-2}$ reduction in critical plasma density enables novel mono-energetic acceleration regimes. These include laser hole-boring through plasma and collisionless electrostatic shock wave acceleration.

Section 4 explores the potential of LWIR lasers to drive secondary radiation sources ranging from RF waves to gamma rays.

- Section 4.1 highlights LWIR lasers' capability in generating intense THz radiation and extending High Harmonic Generation (HHG) into the X-ray region.
- Section 4.2 starts with reviewing pioneering ATF experiments in inverse Compton scattering (ICS) focused on investigating nonlinear ICS processes and single-shot, phase-contrast tomography. The λ-proportional increase in the number of photons per joule of laser energy positions LWIR lasers as promising tools for these and future advanced applications where we examine the ability of LWIR beams to create intense X-ray and gamma sources via ICS. Such sources can complement synchrotron light sources or serve as particle-to-radiation converters in gamma colliders.

Section 5 reviews the capability of LWIR lasers to confine terawatt power into a single filament, allowing the laser beam propagation over long distances through the atmosphere. This unique feature also establishes LWIR lasers as powerful tools for remote diagnostic applications.

- Section 5.1 addresses the terawatt LWIR radiation channeling through air and its observation in ATF experiments.
- Section 5.2 describes secondary effects and applications that emerge from LWIR filaments, including remote detection of ionizing sources and RF waves generation.

In Conclusions, we summarize the main points of this review and briefly address our experience in using LWIR lasers in broader studies not covered by this paper.

2. Short-Pulse LWIR Lasers with CO_2 Amplifiers

Steady progress in ultrafast solid-state laser technology and frequency conversion techniques—such as optical parametric chirped-pulse amplification (OPCPA) and difference-frequency generation (DFG)—has made it possible to achieve multi-gigawatt peak powers in the LWIR range, with pulse energies on the order of tens of microjoules [5]. Theoretically, it is predicted that terawatt peak powers in sub-cycle pulses can be attained [6]. However, reaching pulse energies at the joule scale is currently only feasible through amplification in high-pressure CO_2 laser amplifiers [2,7]. Therefore, this section focuses on the research and development of this class of LWIR laser systems.

2.1. History and State-Of-The-Art

Unlike NIR solid-state lasers, which generate radiation through stimulated transitions between electronic energy levels, LWIR gas lasers operate via transitions between closely spaced energy levels associated with molecular vibrations. CO_2 gas lasers are a prime example of this class, notable for their high efficiency in converting pump energy into laser radiation.

High-pulse-energy CO_2 lasers, with large active volumes, are typically pumped either by low-energy electrons from an electric discharge within the active gas medium or directly by high-energy electron beams originating outside the active volume [8]. These pumping techniques enable the production of laser pulses with energies reaching several kilojoules.

One prominent example is the Antares CO_2 laser, constructed at Los Alamos National Laboratory in the 1980s for a nuclear fusion project. At the time, it was the most powerful laser in the world, producing multiple beams with a combined total energy of 100 kJ at a wavelength of 10.2 μm. This output was achieved using 24 laser amplifiers, each with an active volume of approximately 300 L [9].

The Antares system demonstrated the immense potential of CO_2 lasers for high-output energy scaling. However, due to the discrete gain spectrum shaped by the rotational structure and other physical and technical constraints, mode-locking techniques that enable the generation of picosecond and femtosecond pulses in solid-state lasers [10] are less effective for molecular gas lasers. Consequently, the pulse duration of the Antares laser was limited to 2.5 ns, resulting in a peak power of 1.5 TW per beam.

Later technological advancements introduced an alternative pulse-forming technique that involved "slicing" a short seed $\lambda \approx 10$-μm pulse using the method of semiconductor optical switching driven by a mode-locked solid-state NIR laser [11]. This approach allows us to reduce the CO_2 laser pulse duration to a few picoseconds. However, the challenge persisted: the rotational structure imposed on the spectral envelope of the amplified short pulse caused the picosecond pulse to fragment into a long pulse train [1].

The issue of pulse splitting was resolved by applying two methods: collisional broadening of CO_2 molecule rotational lines by increasing the gas pressure [12] and introducing the ^{18}O isotope into the gas mixture [13]. A combination of these measures resulted in spectral gain smoothing due to the double action of collisional broadening and small shifts in the overlapping spectra of the components in the stoichiometric mixture

$C^{16}O_2$:2($C^{16}O^{18}O$):$C^{18}O_2$. This approach, implemented in the laser amplifier system at the ATF, effectively eliminated pulse trains, delivering a single picosecond pulse [14].

However, the achievable peak power was constrained by self-phase modulation at the output window of the final amplifier [15]. To overcome this limitation, the CPA technique [4] has been implemented, marking its first application to molecular gas lasers. This innovation enabled the generation of single 2 ps pulses with a peak power of 5 TW at λ = 9.2 µm [16,17], using a relatively compact final amplifier with a 10 L gas discharge volume. This achievement stands as the highest power ever attained by an LWIR laser in a solitary-pulse format.

This state-of-the-art LWIR laser system, shown in Figure 1, operates at the ATF to support multidisciplinary user experiments. It features an all-solid-state optical parametric amplifier (OPA) front end, which provides the seed pulse to the CO_2 laser amplifiers. Notably, the semiconductor optical switching technique is still employed, but in this instance, it is used exclusively for extracting an amplified LWIR pulse from the regenerative pre-amplifier cavity.

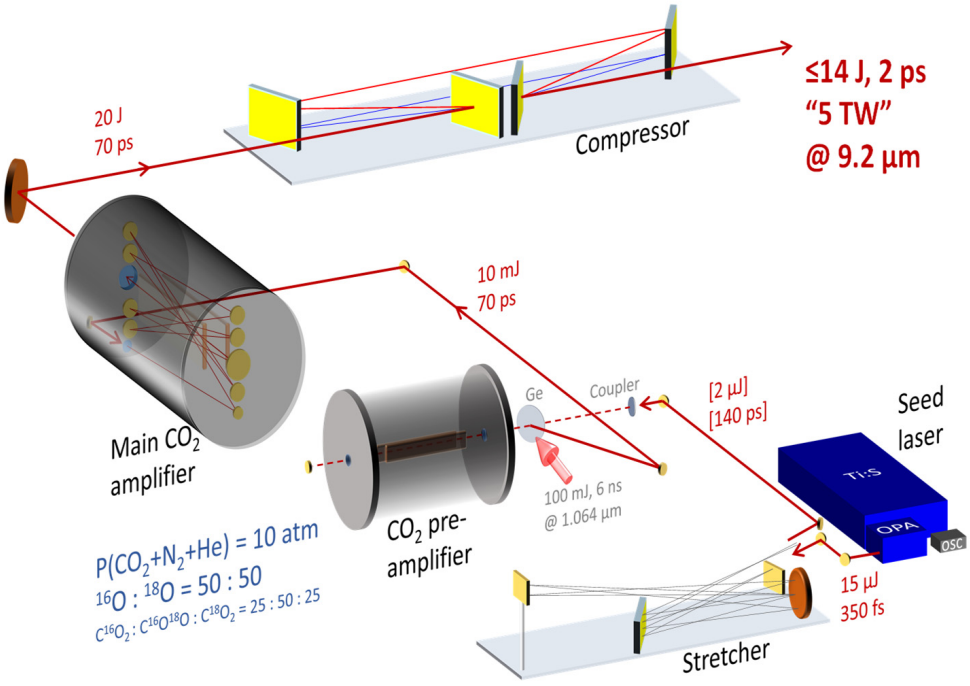

Figure 1. Diagram of the ATF LWIR laser [17]. The system features an all-solid-state optical parametric oscillator amplifier (OPA) front end, high-pressure isotopic CO_2 laser amplifiers operated at a CPA regime, which is enabled by a stretcher-compressor combination based on diffraction gratings. A detailed description of this system can be found in Ref. [16].

2.2. Paths to Femtoseconds

The ~1 THz bandwidth of the strongest branch of the CO_2 radiation spectrum, 9R, centered at 9.2 µm, is equal to that of a transform-limited 500 fs pulse. However, the minimum achievable pulse duration of an amplified pulse is presently restricted to 2 ps due to gain narrowing. This effect arises from the extremely high amplification (~10^{11}) required to increase the pulse energy from microjoules to the multi-joule level (~10^7 net amplification), while compensating for optical losses in the system (~10^4). These losses occur primarily during the pulse injection, extraction, and 16 round-trips within the regenerative CO_2 preamplifier. These high amplification levels make the system highly sensitive to even small variations in the gain spectrum profile, effectively filtering out a relatively narrow ~220 GHz region corresponding to a 2 ps transform-limited pulse.

A significant reduction in gain narrowing can be achieved by employing a seed pulse with sufficiently high energy, thereby eliminating the need for a regenerative pre-amplifier. The first two columns in Figure 2 present numerical modeling of amplification under two scenarios: the current setup, where a 1 μJ, 1 ps seed pulse is amplified using a regenerative pre-amplifier and final amplifier combination; and a preferred configuration, where a 10 mJ, 300 fs pulse is directly seeded into the main amplifier of the ATF laser system [17]. In both cases, the seed pulse is initially stretched to approximately 100 ps before amplification and subsequently compressed to its transform-limited duration after amplification. By mitigating gain narrowing and utilizing the combined spectral bandwidths of the 9R and 9P branches for the 10 mJ, 300 fs seed pulse, the output pulse duration can be recompressed to approximately 500 fs. This approach significantly enhances system performance, effectively increasing peak power nearly fourfold compared to the current configuration.

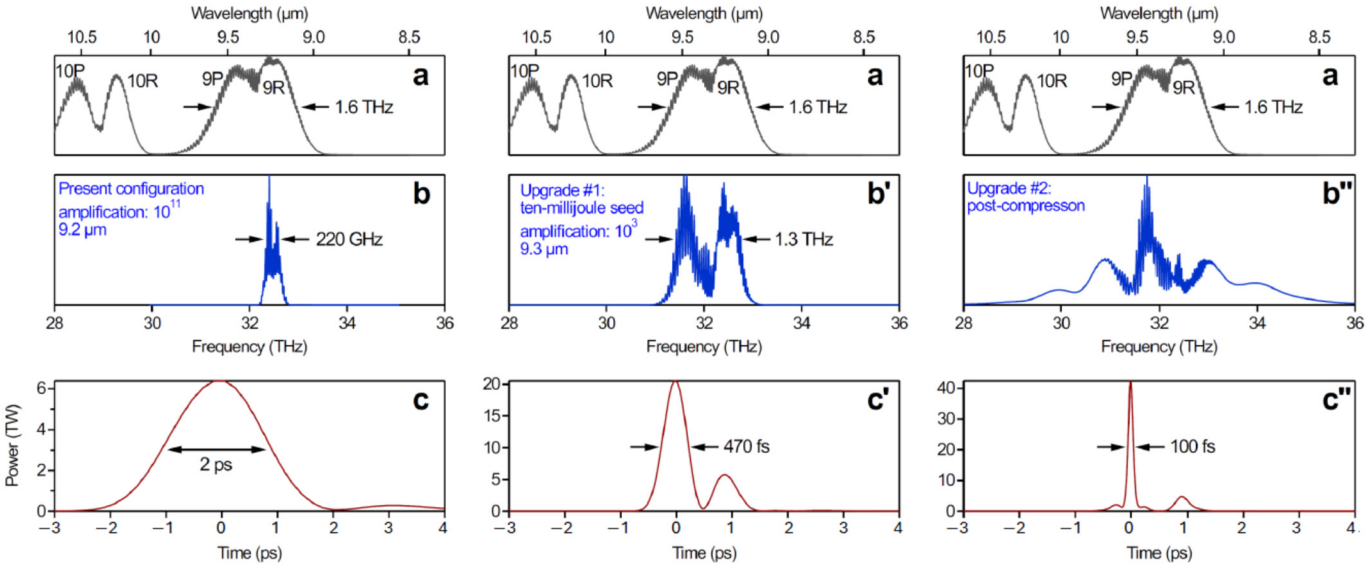

Figure 2. Simulations of short LWIR pulse amplification in the ATF laser system: (**a**) the normalized gain spectrum of the final amplifier; (**b**) the normalized spectrum of the pulse amplified from a 1 μJ, 1 ps seed using the combination of a regenerative pre-amplifier and the final amplifier; (**c**) the temporal profile at the system's output for a 1 μJ, 1 ps seed; (**b′**) the normalized spectrum of the amplified pulse starting from a 10 mJ, 300 fs pulse seeded into the final amplifier; (**c′**) the temporal profile at the system's output for a 10-mJ, 300-fs seed; (**b′′**) the normalized spectrum of the post-compressed pulse; and (**c′′**) the temporal profile of the post-compressed pulse [18].

Reducing the LWIR laser pulse duration to 500 fs or shorter, while increasing the peak power beyond 10 TW, is essential for accessing strongly relativistic regimes of laser-matter interaction [19]. Several schemes for generating energetic LWIR seed pulses are currently under investigation. One approach involves Raman scattering in a calcite crystal, followed by difference-frequency generation between the Raman-shifted and fundamental frequencies [10,20]. Another promising method is a multi-stage optical parametric chirped pulse amplification (OPCPA), pumped by a mid-wave IR (~2–4 μm) laser [7,21].

A complementary approach to CO_2 laser-pulse compression to femtoseconds beyond the bandwidth limit of the active medium involves using self-phase modulation (SPM) in a medium to broaden the pulse's spectrum and chirp its carrier frequency.

The first observation of millijoule, picosecond pulse compression to ~600 fs was reported by Paul Corkum in a high-pressure CO_2 laser amplifier [22]. This effect was attributed to spectral broadening of the pulse via an SPM process in the amplifier's discharge plasma, followed by compression due to negative group velocity dispersion (GVD) in the amplifier's NaCl windows. However, while this method is suitable for direct short

pulse amplification, it is likely incompatible with the CPA technique, which is essential for amplifying CO_2 laser pulses to the joule level and beyond.

Post-compression methods, widely employed with CPA NIR lasers, utilize SPM induced by the Kerr effect in an optical material or a gas-filled capillary [23–25]. Placed in the laser output beam path, this nonlinear optical component functions as a bandwidth expander, introducing a quasi-linear frequency modulation across the pulse's temporal envelope. The resulting positive frequency chirping enables further pulse compression using a diffraction grating, a chirping mirror, or an optical material with negative GVD.

Sub-picosecond post-compression has been experimentally explored in the mid-wave IR at λ = 3.1 μm [26] and λ = 3.9 μm [27], as well as theoretically in the LWIR at $\lambda \approx 10$ μm [28–30]. Numerical simulations have suggested the possibility of compressing 2.5 ps, 500 GW CO_2 laser pulses down to 250 fs by leveraging the nonlinear and dispersive properties of bulk NaCl crystals [28].

This proposed regime was experimentally tested at the ATF, where pulse spikes as short as 130 fs were observed after propagating a ~1 TW, 2 ps, λ = 9.2 μm CO_2 laser beam through a 10 cm thick NaCl slab. The experimental results validated the simulation model, which accurately predicted these temporal structures [31]. However, a significant limitation was also identified: the reliance on simultaneous SPM and dispersive compression (DC) within the same optical element restricted the potential for process optimization. Additionally, micro-filamentation observed within the NaCl slab disrupted beam uniformity.

This limitation prompted the exploration of alternative materials to improve pulse compression by partially separating the post-compression process into two consecutive stages: SPM and DC. Extensive material studies—including measurements of nonlinear refraction index (n_2), nonlinear absorption, damage thresholds, and other material responses to high-power irradiation—led to the identification of potassium chloride (KCl) and barium fluoride (BaF_2) as a promising material combination for post-compression [32].

By implementing this approach, combined with optical filtering between the SPM and DC stages, the compression of 330 mJ pulses from 2 ps to 350 fs was demonstrated in a small-scale proof-of-principle experiment (see Figure 3) [33].

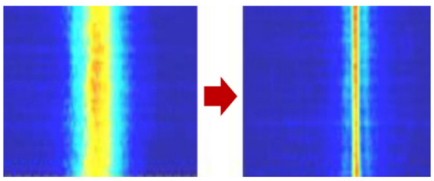

Figure 3. Single-shot autocorrelator images illustrate the 9.2 μm pulse compression from 2 ps to 350 fs in a proof-of-principle ATF experiment [33].

In a follow-up experiment, a 675 fs pulse with a 1.6 TW peak power was achieved, marking it the most powerful femtosecond LWIR laser demonstrated to date [34]. Current efforts are focused on achieving a 5 TW output with a 560 fs pulse by fully utilizing the output capacity of the existing ATF LWIR laser system.

The ultimate goal is to combine the two techniques discussed—a strong seed pulse and post-compression—to produce a few-cycle laser pulse with peak power in the hundreds of terawatts. Numerical modeling for this setup is shown in Figure 2b″,c″. These results correspond to the post-compression of the pulse with parameters shown in Figure 2b′,c′. Notably, the 100 fs pulse spans only three cycles of laser oscillation, highlighting its significant potential for applications such as the generation of sub-cycle THz radiation and HHG sources (see Section 4.1).

Accurate pulse characterization techniques play a crucial role in advancing the development of shorter and more powerful pulses. However, commercially available diagnostics

for the LWIR range lag behind those available for the near-IR range. This gap primarily stems from lower current demand, expected to increase as LWIR lasers mature, rather than from fundamental technological limitations. Consequently, in-house-built diagnostics like SHG-based autocorrelators and grating spectrometers are frequently deployed on an as-needed basis.

2.3. High Repetition Rate Prospects

Presently, the ATF laser's repetition rate is restricted to a few shots per minute. This limitation is primarily due to the high-pressure air spark gaps used as high-voltage switches in the multi-stage Marx generator, which delivers several kilojoules of electrical energy in pulses of up to 800 kV to sustain the electrical discharge in the final amplifier.

Many laser applications would benefit from significantly higher repetition rates. While no direct prototype for a high-repetition-rate, high-voltage driver compatible with the electric-discharge pump parameters of the ATF's laser amplifier currently exists, a potential solution could involve replacing the air spark gaps with thyristors, which can operate at frequencies of up to 350 Hz [19].

Meanwhile, smaller-scale, high-pressure CO_2 lasers with repetition rates in the hundreds of hertz are commercially available [35]. These lasers utilize pulse-forming networks driven by thyratrons, which provide reliable, long-lifespan performance. However, the lower voltage output of thyratron-based pulse generators limits these lasers to smaller active volumes, rendering them unsuitable for achieving multi-terawatt peak power in a single beam. Nonetheless, they are well-suited for applications requiring lower peak power but high average power.

Moreover, operating a laser in pulse-burst mode, where the laser produces a train of pulses from a single electric discharge, effectively multiplies the cumulative repetition rate. This pulse format has been proposed for driving high-brightness ICS radiation sources, achieved by counter-propagating a CO_2 laser beam and an electron beam circulating in a high-repetition storage ring or in energy recovery linac [36].

Operating at a discharge repetition rate of 100 Hz and delivering trains of 100 pulses per shot, the proposed laser system is expected to provide 3 kW of average power at a cumulative repetition rate of 10 kHz. Such a laser could enable the conversion of relatively compact, modern electron accelerators into radiation sources that rival or surpass the capabilities of third-generation synchrotron light sources in the hard X-ray region (above 50 keV) [36]. For further discussion of this approach, see Section 4.2.2.

Other advanced concepts for compact, high-repetition-rate, short-pulse CO_2 laser systems explore optical pumping as a promising alternative to electric discharge pumping. One significant advantage of optical pumping is that it eliminates the constraints on selecting specific gas compositions and pressure levels needed for a uniform electric discharge—limitations that otherwise impair the performance of conventional electric-discharge gas lasers. In contrast, an optically pumped amplifier cell can be filled with pure CO_2 gas at extremely high pressure. Additionally, it offers a compact design due to its high pump-to-lasing conversion efficiency and high gain coefficient.

Several schemes compatible with high-repetition-rate operation have been explored for optical pumping of CO_2 molecules, some of which were successfully demonstrated decades ago using chemical gas lasers [37,38]. These early experiments showed the feasibility of exciting a CO_2 active medium at very high pressures, the flexibility in selecting the gas mixture, significant quantum efficiencies, and the ability to maintain very high gains, up to 10%/cm. The most efficient scheme involved direct pumping of the upper CO_2 laser level at the 4.3 μm wavelength using the HF chemical laser [38].

More recently, several scenarios for optical pumping of CO_2 molecules using solid-state lasers have been proposed. Among the most promising developments is the introduction of an Fe:ZnSe laser, tunable in the 3.9–5 μm range. The best results achieved so far with this laser at 4.3 μm are approximately 50 mJ in 200 ns pulses at a repetition rate of 3 Hz, with the potential to deliver several joules from cryogenically cooled Fe:ZnSe crystals [39]. The next step would involve creating a 10 Hz Fe:ZnSe laser capable of delivering 4 J in 100 ns pulses. Scaling such a laser to a 1 kHz repetition rate is considered feasible. Simulations suggest that this pump would be sufficient to energize very compact 15 atm CO_2 amplifiers, delivering 0.5 J, 0.5 ps pulses in the LWIR [40].

3. Plasma Accelerators

3.1. Wavelength Scaling in Laser–Plasma Interactions

To facilitate further discussion on the applications of LWIR lasers in plasma accelerators, we will first address the basic effects related to laser beam propagation in plasma and their dependence on the laser wavelength.

3.1.1. Ionization

Direct atomic ionization is typically inaccessible with LWIR and even NIR photon energy. However, at high laser intensities, indirect ionization processes become significant, including multiphoton ionization and tunneling (or barrier suppression) ionization. The borderline between these two regimes is characterized in terms of the well-known Keldysh parameter [41]:

$$\gamma_K = \sqrt{\left(\frac{\epsilon_i}{2U_p}\right)},$$

where ϵ_i is the ionization potential energy and U_p is the energy acquired by electron oscillating in the EM field:

$$U_p = \frac{e^2E^2}{4m_e\omega^2}$$

with e being the electron charge, E the electric field amplitude, m_e the electron mass, c the speed of light in a vacuum, and ω the laser frequency related to the wavelength by $\omega = 2\pi c/\lambda$.

The condition $\gamma_K \gg 1$ corresponds to the situation when the ionization potential significantly exceeds the energy gained by an electron within the laser field. In this regime, ionization occurs through a multiphoton absorption process, where electrons absorb successive photons, accumulating energy until they surpasses the binding potential, leading to ionization. This process typically dominates in high-frequency fields with relatively "weak" amplitudes.

The condition $\gamma_K \ll 1$ is satisfied when the electric field becomes strong enough to suppress the Coulomb barrier, significantly increasing the probability of electron tunneling. As the field amplitude increases, the tunneling time decreases, eventually allowing tunneling to occur within a single laser period—a process known as barrier suppression ionization. Notably, at a fixed field amplitude, increasing the laser wavelength by a factor of ten results in a hundredfold increase in the energy acquired by the oscillating electron. Consequently, long-wavelength radiation is inherently more effective at overcoming this potential barrier. For instance, in the case of CO_2 laser radiation ionizing H_2 gas, the condition $\gamma_K = 1$ is satisfied at the laser peak intensity $I \approx 1$ TW/cm^2, with full ionization occurring at approximately $I \approx 100$ TW/cm^2.

At relatively high gas densities—conditions of particular interest for laser–plasma accelerators—avalanche ionization via electron collisions may become one of the primary mechanisms for achieving a fully ionized plasma, starting from initial field ionization or

a small number of seed electrons. A free electron oscillating in the laser field gains an average energy of U_p. However, it can reach the ionization energy ϵ_i by incrementally accumulating kinetic energy in steps of $U_p/2$ during collisions with neutral molecules. Once again, because $U_p \sim \omega^{-2}$, avalanche ionization proceeds more rapidly in a slowly oscillating field. The time to the full ionization, τ_{ion}, scales as $\tau_{ion} \sim \epsilon_i \omega^2 / I$ [42]. For instance, with a CO_2 laser at an intensity of 100 TW/cm^2, it takes only about 100 fs to reach the critical plasma density of 10^{19} cm^{-3} in 1 atm H_2 gas.

3.1.2. Critical Plasma Density

An EM field with the frequency ω propagating through plasma with the electron density n_e must satisfy the dispersion relation,

$$k = \frac{\omega}{c}\sqrt{\left(1 - \frac{\omega_p^2}{\omega^2}\right)},$$

where $k = 2\pi/\lambda$ is the wavenumber, $\omega_p = \sqrt{n_e e^2 / m_e \varepsilon_0}$ is the electron plasma frequency, m_e and e are the electron mass and charge, n_e is the electron plasma density, and ε_0 is the vacuum permittivity.

Rearranging the expression for ω_p under the condition $\omega = \omega_p$, we derive the critical electron plasma density:

$$n_{cr} = m_e \varepsilon_0 \omega^2 / e^2 \equiv \omega^2 / 4\pi c^2 r_e,$$

where r_e is the classical electron radius. Beyond this critical density, the EM wave cannot propagate. Physically, this condition means that when $\omega < \omega_p$, the plasma electrons respond quickly enough, and their density is high enough to generate local compensating fields that cancel the EM field, preventing its further propagation.

Later, we will examine how the proportional reduction in n_{cr} by ω^2 for LWIR beams impacts laser-driven electron and ion acceleration in plasma.

3.1.3. Laser Self-Focusing and Channeling

When propagating through a uniform plasma, a high-peak-power laser beam causes plasma electrons to oscillate with relativistic velocity. The onset of the relativistic oscillatory motion is expressed by the condition $eE = m_e c\omega$. By using the expression, $E = \sqrt{2I/\varepsilon_0 c}$ and the corresponding engineering formula $E[\mathrm{TV/m}] \approx 2.75 \times \sqrt{I[\mathrm{TW/cm^2}]}$, we conclude that, for λ = 10 μm, the onset of relativistic electron motion occurs at $I = 1.4 \times 10^{16}$ W/cm^2, compared to $I = 1.4 \times 10^{18}$ W/cm^2 at λ = 1 μm.

Relativistic motion increases the effective mass of electrons, making them "heavier" by a factor called cycle-averaged Lorentz parameter $\langle\gamma\rangle = \sqrt{\left(1 + \frac{j a_0^2}{2}\right)}$, where $j = 1$ for linear polarization and $j = 2$ for circular polarization. Here, a_0 is the dimensionless laser vector-potential

$$a_0 = eE/m_e c\omega \approx 0.3E[\mathrm{TV/m}]\lambda[\mu\mathrm{m}] \approx 0.855\sqrt{I_{18}}\lambda[\mu\mathrm{m}],$$

where I_{18} represents the laser intensity measured in 10^{18} W/cm^2.

The relativistic increase in electron mass reduces the plasma frequency ω_p and increases the plasma's refractive index $\eta = \frac{ck}{\omega} = \sqrt{\left(1 - \frac{\omega_p^2}{\omega^2}\right)}$. The resulting radial variations in the local plasma refractive index caused in plasma by a gaussian beam act as an effective positive lens, counteracting the natural diffraction divergence of the laser beam

when laser peak power reaches the relativistic self-focusing (RSF) threshold, given by $P_{RSF} \approx 17\left(\frac{\omega}{\omega_p}\right)^2$[GW] [43].

We see that at a fixed plasma density, LWIR lasers require much less power to reach the RSF threshold compared to NIR lasers. For instance, at $n_e = 10^{17}$ cm^{-3}, the RSF condition is satisfied with a ~28 TW CO_2 laser, in contrast to the ~3.8 PW required for a TiS laser.

Other contributions to the lensing effect via plasma density redistribution include thermal and ponderomotive effects, which arise from the expulsion of electrons from regions of high laser intensity. Thermal effects occur as the intense laser heats the plasma, creating density gradients due to thermal expansion. On the other hand, the ponderomotive force,

$$m_e \frac{\partial v}{\partial t} = -\frac{e^2}{4m_e\omega^2}\nabla E^2,$$

which will be addressed below in more detail, arises from the spatial variation in laser intensity ∇E^2, driving electrons out of high-intensity regions. Ions subsequently follow the electrons but at a slower pace.

Since thermal and ponderomotive plasma density modulation occur on a slower timescale compared to RSF, these effects become more pronounced for relatively long laser pulses. They are also crucial for creating preformed plasma channels using pilot lasers, which can then guide the main laser beam more effectively.

Regardless of how the plasma channel is formed, whether by another laser or, alternatively, by an electric discharge in a gas-filled or ablative capillary, the waveguiding condition

$$\Delta n_e \geq \left(\pi r_e w_0^2\right)^{-1}$$

where w_0 is the radius of the laser focus, arises from the compensation of laser beam diffraction divergence through total internal reflection, caused by a radially variable plasma refractive index [44]. Substituting constants, this simplifies to

$$\Delta n_e[\text{cm}^{-3}] \geq 1.13 \times 10^{20}/w_0^2[\mu\text{m}].$$

This laser guiding condition in a preformed plasma channel is not sensitive to the laser wavelength. Therefore, plasma channel techniques developed and optimized for NIR beams [44–47] can also be effectively applied to guiding LWIR beams, as has been demonstrated in the ATF experiment [48].

3.1.4. Laser Energy Loss on Propagation

As a laser pulse propagates through plasma, it loses energy via several absorption mechanisms, which depend both on the laser intensity and plasma density. When a laser pulse interacts with plasma at an over-critical density ($n_e > n_{cr}$ or $\omega < \omega_p$), energy coupling into the plasma typically occurs over the spatial scale of the skin depth, c/ω_p. This depth defines the distance over which the electric field amplitude decreases by a factor of $1/e$. Beyond this skin depth, the external electric field is effectively screened. Within this thin layer, copious hot electrons are generated, with average thermal energy approximately equal to the ponderomotive potential, $k_B T_e \approx U_p$, where T_e is the electron temperature and k_B is the Boltzmann constant. The efficiency of laser energy transfer to hot electrons increases with laser intensity, reaching 60–90% for relativistic laser beams ($a_0 > 1$). In the context of this paper, these conditions are particularly relevant to ion acceleration, as hot electrons propagating beyond the skin layer produce electrostatic potential that draws positive ions forward.

In sub-critical plasma ($n_e < n_{cr}$), inverse bremsstrahlung—where EM energy is transferred to free electrons—may become a predominant absorption mechanism [49]. Similarly

to the avalanche ionization process, electrons heated by the laser transfer their energy to neutral or ionized atoms through collisions, continuously depleting the laser beam's energy.

This process determines the laser depletion distance

$$L_D = \frac{\omega^2}{\omega_p^2}\frac{c}{\nu_{ei}},$$

where $\nu_{ei} = n_i v\sigma$ is the electron–ion collision frequency, n_i is the ion density, v is the electron velocity, and σ is the cross-section for momentum transfer collisions [50]. For typical hydrogen plasma conditions, $v\sigma \approx 1.6 \times 10^{-7}$ cm^3 s^{-1} [51,52].

It follows that L_D scales with n_e^{-1}, and for a wavelength of λ = 10 µm, it increases from 2 cm at 10^{18} cm^{-3} to 2 m at $n_e = 10^{16}$ cm^{-3}.

3.2. Electron Acceleration in Plasma Waves

When propagating in a sub-critical plasma, a laser pulse excites a plasma wave through the following mechanism: The electron excursion over a single cycle of its oscillation in the laser's EM field depends on the field amplitude and frequency. The spatially varying laser intensity profile causes an inequality in these excursions. For electrons near the peak of the intensity profile, the restoring force in the second half of the laser cycle is reduced, leading to a time-averaged net force, known as the ponderomotive force. This net force pushes electrons collectively away from regions of higher intensity [53,54].

As electrons are displaced by the ponderomotive force, the remaining positive ions exert a Coulomb restoring force. This interaction induces collective electron oscillations at the plasma's eigenfrequency, ω_p. The resulting plasma wake co-propagates with the local group velocity of the laser pulse.

3.2.1. Regimes of Laser-Driven Plasma Acceleration

The separation of electrons and ions in the plasma wake generates co-propagating longitudinal and radial electrostatic fields. Charged particles riding the proper phase of the wake can be accelerated to relativistic energies. This process is known as laser wakefield acceleration (LWFA) [53,55].

For low laser intensities ($a_0 << 1$), the wake fields are sinusoidal, and the amplitude of the accelerating electric field, E_a, is proportional to the square root of both the laser intensity and the plasma density [53]:

$$E_a[V/\text{cm}] \approx a_0\sqrt{n_e[\text{cm}^{-3}]} \approx 0.855\lambda[\mu\text{m}]\sqrt{I_{18}n_e[\text{cm}^{-3}]}.$$

In this regime, plasma electrons do not gain sufficient momentum to become trapped in the plasma wave, so electrons must be longitudinally injected with an initial energy compatible with the plasma wave velocity.

It is instructive to compare E_a with $E[\text{V/cm}] \approx 8.67 \times 10^{10}\sqrt{I_{18}}$, obtaining the efficiency of converting the transverse EM oscillating field into the longitudinal electrostatic accelerating field in a plasma wake:

$$E_a/E \approx 10^{-11}\lambda[\mu\text{m}]\sqrt{n_e[\text{cm}^{-3}]}.$$

We see that, at a fixed plasma density, a LWIR laser is an order of magnitude more efficient in driving a plasma wake compared to the NIR laser of the same intensity.

At high intensities ($a_0 \geq 1$), the relativistic increase in electron mass by the factor of $\langle\gamma\rangle$ slows the electron down at the peak of its oscillation in the EM field. This leads to the development of a sawtooth profile in the wake field, which ultimately breaks when

the wave-breaking limit $E_a^{wb} = m_e c\omega_p/e$ is reached [53,54,56]. For example, for a plasma density $n_e = 10^{16}$ cm^{-3}, we find $\omega_p = 5.6 \times 10^{12}$ s^{-1} and $E_a^{wb} = 10$ GV/m. At the top of the breaking wave, some plasma electrons gain significant longitudinal momentum due to a local field turbulence. They can be self-injected and trapped in a plasma wake for continuous acceleration.

Plasma wakes are most efficiently generated when the characteristic timescale of collective plasma electron motion—displaced by the leading edge of the laser pulse and returning at its trailing edge—matches the wakefield period. This condition is met when the laser pulse duration satisfies $\tau\omega_p \approx 1$ [57].

For long pulses out of resonance ($\tau\omega_p > 1$), the initially small-amplitude plasma oscillations may cause periodic modulation of the laser pulse intensity due to two mechanisms: (i) focusing (defocusing) in regions of lower (higher) plasma density; (ii) beating between the driving pulse and the forward Raman-scattered waves at frequencies $\omega \pm \omega_p$. The modulated pulse envelope resonates with the plasma wave, increasing its amplitude, which in turn enhances the laser envelope modulation in the so-called self-modulated regime (SM-LWFA) [58].

The most effective highly nonlinear LWFA regime, known as the "bubble" regime, is achieved with a short laser pulse ($\tau\omega_p \leq 1$) of a power above the wave-breaking threshold. For this regime, the laser pulse focused into the plasma must also satisfy the following conditions for its focal size, w_0, duration, τ, and peak power, P_L [59]:

$$w_0\omega_p \approx c\sqrt{a_0},\ \tau \leq \frac{w_0}{c},\ \text{and}\ P_L > P_{bubble} \approx P_{RSF}(\omega\tau)^2.$$

In this regime, an evacuated cavity free of cold plasma electrons is formed. Electrostatic field distribution inside this cavity is capable of trapping, focusing, and accelerating compact and dense electron bunches self-injected at the rear of the bubble. The energy spectrum of the accelerated electrons is strongly peaked, in contrast to the quasi-thermal spectra typically produced by SM-LWFA. However, auxiliary methods for precision electron injection still offer certain advantages, which will be discussed in detail later.

A fundamental limit to the distance over which particles can be accelerated arises from the fact that the plasma wave travels at the group velocity of the laser pulse, $v_g = c\sqrt{\left(1 - \frac{\omega_p^2}{\omega^2}\right)}$, which is less than the speed of light in a vacuum, c, while the accelerated particles can reach speeds closer to c. As a result, particles slip forward from the region of acceleration to a region of deceleration after propagating a certain distance, known as the dephasing length, $L_{ph} \approx \lambda_p^3/\lambda^2$, where $\lambda_p = 2\pi c/\omega_p$. For λ = 10 μm and $n_e = 10^{16}$ cm^{-3}, the dephasing length L_{ph} is approximately 40 cm.

Another limitation may arise from the depletion of the driving laser through energy transfer to the plasma wave, which is given by the energy depletion length $L_d' = c\tau(E/E_a)^2$ [60]. Under the bubble LWFA conditions, this mechanism dominates over the bremsstrahlung losses estimated previously. When the pulse duration matches the plasma oscillation period, $\tau \approx \lambda_p/c$, the depletion length L_d' becomes comparable to the dephasing length L_{ph}.

3.2.2. SM-LWFA Driven by LWIR Laser

It is instructive to examine the scaling of key normalized input parameters used in plasma accelerator simulations: time $\widetilde{t} = \omega_p t$, length $\widetilde{x} = \frac{\omega}{c}x$, density $\widetilde{n}_e = \frac{n_e}{n_{cr}} \propto \frac{1}{\omega^2}n_e$, and EM field $a_0 \propto \frac{\sqrt{I}}{\omega}$. The results of LWFA simulations conducted in these terms will be independent of the laser wavelength for properly scaled laser and plasma parameters. Consequently, a 10 μm laser can sustain LWFA regimes that are qualitatively identical to

those of a 1 μm laser but achieve this with 100 times less peak power and operating at 100 times lower plasma density. As we will see, this scaling offers substantial advantages for certain applications.

The 5 TW LWIR (9.2 μm) laser available at the ATF, exceeds the P_{RSF} threshold at plasma densities as low as 5×10^{16} cm^{-3}, enabling LWFA experiments that would otherwise require a 170 TW 1 μm laser [61]. Although these opportunities were predicted theoretically [62,63], their experimental realization has only been reported recently [64].

The ATF plasma acceleration experiment generated MeV electrons using laser pulses at peak powers both above and below the RSF threshold [64]. These findings demonstrated that self-focusing was no longer essential for exciting plasma wakes or for capturing and accelerating plasma electrons. At plasma densities $n_e \leq 4 \times 10^{17}$ cm^{-3} and the laser peak powers as low as 0.5 TW, collimated quasi-monoenergetic electrons were observed alongside the typically divergent, thermal electrons generated by SM-LWFA. This indicates that researchers had entered a transitional LWFA regime, intermediate between SM-LWFA and bubble [59], also referred to as the "forced" [65] regime.

Notably, this transitional regime was observed at plasma densities approximately 100 times lower than those typically achieved in earlier experiments using $\lambda \approx 1$ μm lasers [65] or in more recent studies with $\lambda = 3.9$ μm lasers [66]. This breakthrough marks a critical step toward realizing the LWFA bubble regime at unprecedently large spatial scales in plasma densities of $n_e \approx 10^{16}$ cm^{-3}. Such regime holds significant promises for the precise injection of low-energy-spread, low-emittance electron bunches from conventional linacs into the LWFA stages, with strong potential for maintaining high beam quality throughout the acceleration process. ATF, with its 75 MeV photocathode linac synchronized to the LWIR laser, is well positioned for advancing these studies.

Additionally, ATF plasma acceleration experiments have provided new insights into the characteristics of generated wake fields by utilizing short electron bunches from the ATF's linac, directed perpendicular to the laser beam. These bunches create "frozen" radiographic images of plasma fields on a luminescent screen positioned at a variable distance from the wake. This technique offers a rare opportunity to visualize wake fields, which are otherwise understood primarily through simulations.

Figure 4 illustrates this approach, comparing experimental and simulated electron beam (e-beam) patterns produced by a collimated e-beam traversing a wake generated by a CO_2 laser [67]. By recording the e-beam's focal positions on the screen, this method enables researchers to map the morphology of radial-focusing fields at each transverse cross-section of the wake.

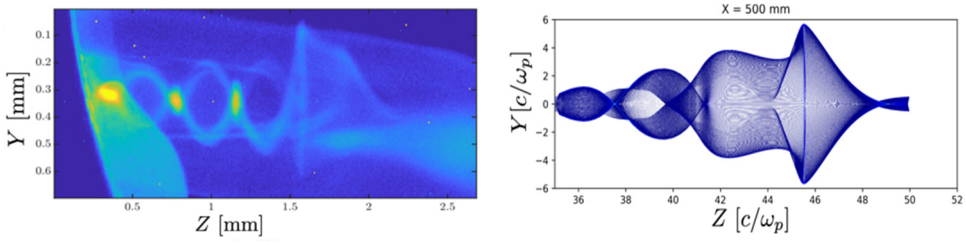

(**a**) (**b**)

Figure 4. Experimentally observed (**a**) and simulated (**b**) electron beam patterns 50 cm downstream from a wake field generated in $n_e = 10^{15}$ cm^{-3} plasma by a 2 TW, 2 ps CO_2 laser pulse [67].

3.2.3. Low-Density Bubble Regime

Demonstrations of high-energy electron bunches from laser-driven plasma wakefield accelerators represent one of the most successful applications of NIR CPA lasers. Those experiments confirmed the bubble regime as the most promising approach for constructing

compact LWFA stages. Acceleration gradients approaching 1 GeV/cm have been demonstrated, with net electron energies reaching approximately 10 GeV. This was achieved by sustaining acceleration over distances of 10–20 cm using ~1-PW NIR laser beams, either through waveguide-assisted laser channeling [68] or relativistic self-focusing [69]. These experiments utilized TiS or Nd laser systems, delivering 30–130 J in 35–135 fs pulses at wavelengths of λ = 0.8–1.06 μm, focused into hydrogen gas and reaching intensities corresponding to $a_0 \approx 3$. These setups generated plasma bubbles approximately 50 μm in size at electron plasma densities of (3–6) $\times 10^{17}$ cm^{-3}. Accelerated electron bunches carried up to 60 pC in the self-injection regime [68] and as much as 340 pC using nanoparticle-assisted ionization injection [69].

The results of these experiments are often considered in the context of developing accelerator stages for a prospective high luminosity e^-e^+ collider with up to several TeV center-of-mass (c.m.) energy. Such a collider would open new frontiers in exploring physics beyond the current reach of the Large Hadron Collider (LHC). According to the recommendations of the 2023 Particle Physics Project Prioritization Panel (P5) [70], its design could be based on advanced accelerator concepts, including laser-driven plasma accelerators.

The key characteristic of the collider is the beam luminosity, given by

$$\mathcal{L} = \frac{f N_e^2}{4\pi\sigma_\perp^2},$$

where f is the bunch repetition rate, N_e is the number of electrons (positrons) per bunch, and $\sigma_\perp$ is the averaged transverse beam size at the collider interaction point (IP). For example, satisfying the luminosity $\mathcal{L} \approx$ 10^{35}–10^{36} s^{-1} cm^{-2} targeted for a 10 TeV c.m. collider requires the production of highly reproducible, high-charge (~0.3 nC) electron bunches at a repetition rate of ~1 kHz and focused to $\sigma_\perp$ = 1 nm [70–72]. This demands a low normalized emittance of $\epsilon_n \approx 0.1$ mm.mrad which is defined as

$$\epsilon_n = \frac{(\text{beam size}) \times (\text{beam divergense})}{\gamma}.$$

Additionally, each beam should have a low energy spread of $\Delta\varepsilon_e < 1\%$ [70–72]. Achieving these specifications represents an order-of-magnitude improvement over current electron beam parameters demonstrated in the self-injection bubble LWFA regime.

It has been proposed that the required bunch qualities could be most effectively achieved through precise external electron injection into the bubble within a quasilinear blowout regime, operating below the wave-breaking and self-injection thresholds. This regime can be realized by maintaining a relatively low normalized vector potential ($a_0 \approx$ 1–1.5) and a laser peak power slightly exceeding the self-focusing threshold (P/P_{RSF} = 1.1) [71]. This approach enables greater control over the phasing, acceleration, and focusing field components, making it particularly well-suited for the acceleration of both electrons and positrons.

Furthermore, achieving this goal could be facilitated by using low-density plasma. The improved emittance and energy spread are expected to scale proportionally to λ_p^{-1}, due to a better phase-space fit for seeded electrons within the bubble. Furthermore, the number of trapped electrons and accelerated charges can increase proportionally to λ_p. This scaling of beam parameters makes the low-plasma density regime increasingly attractive for future e^-e^+ TeV-class colliders, which, in addition to requiring high beam quality, also demand a significant bunch charge.

Due to their strong ponderomotive force, LWIR lasers might be efficient in driving plasma wakes in low-density plasmas, such as $n_e \approx 10^{16}$ cm^{-3} [19]. Currently, the shortest high-power CO_2 laser pulses achieved exceed the oscillation period ($\lambda_p/c \approx 1$ ps) for

a plasma wave at n_e = 10^{16} cm^{-3}, failing to meet the optimum conditions for exiting the bubble regime. However, this regime is becoming attainable with only a fourfold improvement over the current pulse duration. This advancement would enable bubble structures of unprecedented size (~300 μm), providing better control of LWFA and enhanced electron beam quality.

To further explore the comparison between NIR and LWIR laser drivers in LWFA stages, it is useful to examine plasma accelerator performance in regimes that offer the best compromise between laser technology capabilities and future collider requirements.

By keeping the normalized LWFA parameters—a_0, $k_p \times w_0$ and $\omega_p \times \tau$ —constant for any laser wavelength, key scaling lows for LWFA regimes with variable ω_p and ω emerge [71,72]. This approach enabled us to construct the entries in Table 1 for four combinations of λ and n_e [19]. The first two columns of Table 1 closely correspond to the case of $n_e \approx 10^{16}$ cm^{-3}. In the subsequent examples, the plasma density is increased tenfold, with all laser parameters scaled proportionally to maintain the same quasilinear blowout LWFA regime.

Table 1. Comparative parameters for plasma bubble accelerators driven with λ = 0.8 μm and λ = 9.2 μm lasers [19].

Parameter	Value			
Laser wavelength (μm)	0.8	9.2	0.8	9.2
Plasma density ($\times 10^{16}$ cm^{-3})	1.1	1.1	11	11
Plasma wavelength (μm)	313	313	99	99
Laser pulse duration (fs)	390	390	130	130
Laser radius (μm)	200	200	63	63
Laser peak power (TW)	3000	23	300	2.3
Laser energy per stage (J)	1200	9	40	0.3
Electrons per bunch ($\times 10^9$)	12	12	4	4
Accelerating field (GeV/m)	4.3	4.3	12.6	12.6
Stage length (m)	25	0.19	0.79	0.06
Energy gain per stage (GeV)	100	0.75	10	0.075

In our analysis, we assume that electron dephasing can be mitigated by appropriately tapering the plasma density within a single accelerating stage.

From the comparison of the four cases presented in Table 1, we can draw the following observations that underscore trade-offs from employing LWIR versus NIR lasers, as well as different plasma densities, in these plasma acceleration schemes:

- Laser Power Requirements: The LWIR laser demonstrates significantly reduced power requirements compared to its NIR counterpart at equivalent plasma densities, highlighting the longer wavelength efficiency in driving plasma waves. Increasing plasma density leads to reduced power requirements for both lasers.
- Electron Energy Gain: Higher plasma density leads to a greater acceleration gradient. However, the net acceleration per stage decreases due to the inverse quadratic relationship between the laser depletion length and the plasma frequency. The reduced energy requirement for LWIR lasers leads to proportionally faster depletion, resulting in a smaller electron energy gain per stage, necessitating more stages for high-energy applications.
- Bunch charge: While the required laser peak power and energy seem more practically accessible at higher densities, the amount of accelerated charge is reduced.

We shall mention that the selection of N_e could be further constrained by the onset of an effect known as beamstrahlung, which causes radiation losses of particle beam energy when electron and positron beams interact at the collider's IP. This "parasitic" gamma radiation

generates background noise in the detectors surrounding the IP, removes energy from the particle beam, and increases the beam energy spread. In general, beamstrahlung must be limited to fewer than one gamma photon per lepton, and the induced $\Delta\varepsilon_e$ constrained to a few tens of a percent.

In our case, this requirement translates to limiting the number of particles per bunch to approximately $N_e \approx 3 \times 10^9$ [73]. However, given the relatively shallow dependence of both the number of beamstrahlung photons and the induced beam energy spread on the bunch charge ($\Delta\varepsilon_e \propto N_e^{1/3}$), the extent to which beamstrahlung imposes a strict design limit on N_e remains to be fully determined.

Table 1 shows that at a plasma density of $n_e = 1.1 \times 10^{17}$ cm^{-3}, a TiS laser must deliver 40 J of energy per pulse. As derived from the expression for $\mathcal{L}$, maintaining high luminosity requires a repetition rate of at least 1 kHz and an average TiS laser power of 40 kW to drive a single stage—far exceeding the capabilities of current laser technology.

Reducing the plasma density allows to maintain the same luminosity with a reduced laser repetition rate following the proportion $f \propto N_e^{-2} \propto n_e$, assuming the parameter $\sigma_\perp$ remains intact. In this scenario, a 1.2 kJ/pulse Ti:Sapphire laser could, theoretically, sustain acceleration over 20 m, achieving an energy gain of 100 GeV per stage. In contrast, a 9 Joule CO_2 laser pulse depletes after just 20 cm, resulting in a net acceleration of only 750 MeV per stage. However, until significant technological challenges associated with construction of kilojoule-class femtosecond NIR lasers and multi-meter plasma waveguides are resolved, CO_2 lasers—requiring 130 times less energy per pulse—might provide a practical platform for exploring and validating promising high-charge, low-density LWFA regimes.

At the same time, an LWFA test facility operating at low plasma densities will also have significant value as a learning step toward optimizing leading collider designs based on NIR lasers interacting with higher density plasmas. One example of such a utility is identifying requirements and verifying solutions for bunch seeding into the LWFA stages.

A seed electron bunch must meet the size and placement accuracy requirements aligned with the accelerating and focusing phases of the longitudinal and transverse electric fields within the plasma bubble. In a bubble generated in the $n_e \approx 10^{16}$ cm^{-3} plasma, these spatial scales are on the order of several tens of micrometers. Even small deviations from the optimal parameter settings can significantly affect the efficiency of the acceleration process and the final beam quality. Simulations presented in Figure 5 [74] illustrate this relationship, showing how the accuracy of seed electron bunch placement affects its energy spread during acceleration.

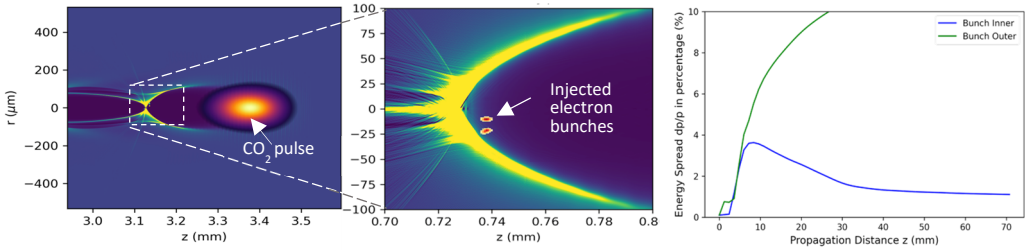

Figure 5. Simulated dynamics of electron bunch energy spread upon acceleration in $n_e = 10^{16}$ cm^{-3} plasma with $a_0 = 4$ CO_2 laser pulse of the 500 fs duration. Inner and outer bunches are injected into the accelerating phase of the bubble 10 μm and 23 μm away from the beam axis, correspondingly [74].

Experimental verification of requirements for bunch seeding into acceleration stages and the preservation of beam quality during acceleration presents key challenges. These studies critically rely on seed electron bunches of high quality—characterized by low energy spread, low emittance, and ideally high charge—to enable comprehensive investigations of

space-charge and beam-loading effects. The ATF, with its high-brightness electron linac, is uniquely positioned to advance these studies.

The ATF's linac is capable of delivering sub-nanocoulomb electron bunches synchronized with a laser to sub-picosecond precision, with transverse and longitudinal dimensions of $\sigma_r = 10$ μm and $\sigma_z = 70$ μm correspondingly. A planned upgrade to the linac's beam transport system aims to further reduce the longitudinal bunch size to 30 μm using a magnetic chicane. These enhanced capabilities are well-suited for conducting high-impact studies on LWFA seeding, acceleration dynamics, and staging, which are essential for advancing the technologies required for future collider initiatives [70].

3.2.4. Ultra-Low Emittance LWFA

Low-density plasma is particularly attractive for designing LWFA-based accelerators capable of achieving ultra-low ϵ_n and $\Delta\varepsilon_e$—parameters that could match or even surpass those of conventional RF accelerators.

One approach to achieving ultra-cold electron bunches from a plasma accelerator is the "two-color" ionization injection method [75,76]. This method has the potential to produce electron bunches with $\Delta\varepsilon_e$ and ϵ_n parameters even better than those achievable with high-brightness photocathode linacs.

In this scheme, the roles of plasma bubble generation and electron injection are separated between two lasers of different wavelengths. A circularly polarized LWIR laser, such as a ~10-μm CO_2 laser, with a normalized vector potential $a_0 \approx 1.2-1.4$ corresponding to a field strength of $E \approx 3.8-4.5$ TV/m, creates a plasma bubble. Simultaneously, a low-power, linearly polarized, femtosecond, short-wavelength laser—such as the second harmonic of a TiS laser at $\lambda \approx 400$ nm—is tightly focused within the plasma bubble trailing the LWIR pulse. Despite a much smaller normalized vector potential $(a_0 \approx 0.1)$, the electric field produced by this short-wavelength laser is significantly stronger ($E \approx 7$ TV/m). This field strength is sufficient to ionize gas components that are otherwise inaccessible to the lower field strength of an LWIR laser. By selectively ionizing these components, the two-color approach enables precise electron injection into the plasma bubble, producing electron bunches with enhanced beam quality.

Simulations indicate that this method can generate electron bunches with sizes on the order of a few micrometers with $\epsilon_n \leq 50$ nm and $\Delta\varepsilon_e \approx 0.1\%$, representing an order-of-magnitude improvement over a single-laser-driven plasma accelerator. These parameters can be preserved during acceleration, provided the injected electron bunch remains sufficiently small to fit within the confined accelerating and focusing phase space of the plasma bubble. Although the charge in the produced micron-size bunches is limited to a few pico-Coulombs—rendering them insufficient for future colliders—these beams are highly relevant for driving next-generation coherent X-ray sources [77].

The ATF, with its combination of LWIR and NIR lasers, is uniquely positioned to implement the two-color LWFA ionization injection method following the completion of its planned LWIR laser upgrade to the sub-picosecond pulse regime, as discussed in Section 2.

3.3. Ion Acceleration

By increasing the electron plasma density, n_e, to n_{cr}, we enter a regime where most of the laser energy is absorbed within a narrow skin depth, accompanied by intense electron heating. As hot electrons escape the skin layer, they create a strong charge separation field, which, in turn, accelerates the remaining plasma ions.

Laser-generated ion beams are regarded as a complement to conventional ion accelerators and radioactive sources, offering high acceleration gradients and efficient conversion of laser energy into ion beam energy.

3.3.1. Solid Targets

Significant progress has been made in generating proton beams through the Target Normal Sheath Acceleration (TNSA) mechanism [78]. This process begins with a high-intensity laser pulse interacting with the front surface of a solid target, such as a thin metal or plastic foil, rapidly ionizing the material and transferring energy to the electrons. Hot electrons are generated at the front surface and ponderomotively accelerated into the bulk of the target, causing further ionization. These electrons gain sufficient energy to escape from the rear of the target into the vacuum, leaving the rear surface positively charged. This charge separation generates an electrostatic sheath field that accelerates ions from the target's surface into the vacuum.

The amplitude of the electrostatic sheath field, which can reach values on the order of MV/μm [79], is described by the formula:

$$E_{sheath} = \frac{\sqrt{2}U_p}{e\lambda_D},$$

where $\lambda_D = \sqrt{\frac{\varepsilon_0 k_B T_e}{n_e e^2}} \propto \sqrt{U_p}$ is the electron Debye length. This length represents the distance over which electrostatic potentials are attenuated to $1/e$ of its original value through collective plasma response. From these relationships, it follows that the sheath field $E_{sheath} \propto \sqrt{U_p}$. The same proportionality applies to the ion velocity, indicating that the energy per nucleon $\varepsilon_p \propto U_p$. Expressing U_p in terms of the dimensionless laser vector potential a_0, $U_p = \frac{a_0^2}{4} m_e c^2$, we conclude $\varepsilon_p \propto a_0$.

The quadratic dependence of a_0 on λ implies that a $\lambda = 10$ μm laser can achieve the same ion energy as a $\lambda = 1$ μm laser but at a hundred times lower intensity. For instance, 1 MeV proton energy can be reached at an intensity of 10^{16} W/cm^2 with a $\lambda = 10$ μm laser compared to 10^{18} W/cm^2 with a $\lambda = 1$ μm laser, as demonstrated in the ATF experiment [80]. Similarly, 200 MeV proton energy may be achievable with intensities of ~10^{20} W/cm^2 in LWIR versus ~10^{22} W/cm^2 in NIR.

The energy transfer efficiency from the laser to the ion beam can reach several percent. Consequently, a laser pulse with just a few joules of energy can generate an MeV ion beam carrying a charge in the tens of nano-Coulomb range.

However, the spectral brightness of these beams is inherently limited by their relatively large angular divergence (~30°) and their thermal Maxwellian energy spectrum, which results from the evolution of the sheath field strength during the laser pulse and the nonuniformity of its surface profile. This poses challenges for applications requiring high spectral purity or precise beam collimation, such as cancer radiotherapy. To achieve the stringent beam quality standards required for these applications, significant spectral filtering and collimation of TNSA beams are necessary, which inevitably leads to beam losses.

Nevertheless, powerful and ultrafast TNSA ion sources hold great promise for other applications, such as proton radiography and neutron production. Their high intensity, low transverse emittance, ultrashort durations—typically on the order of the laser pulse length—and compact size provide distinct advantages in these fields.

The TNSA mechanism is the most efficient when a linearly polarized laser beam strikes the target at a ~45° angle [81]. In contrast, radiation pressure applied by a laser at normal incidence can initiate a different acceleration mechanism known as radiation pressure acceleration (RPA) [82]. This mechanism requires an extremely intense, high-contrast, circularly polarized laser pulse and a very thin, lightweight target, typically with a thickness on the order of the laser wavelength or smaller.

In this scenario, also referred to as the "light sail" regime, the entire target can be set into motion by radiation pressure, $P_{rad} = \frac{1+R}{2}\frac{I}{c}$, where R is the target's reflectivity.

In the non-relativistic limit for a perfect mirror, the final energy per nucleon is given by $\varepsilon_p = 2m_p \frac{I}{\rho c}$, where m_p is the proton mass, and ρ is the target's mass density [83].

By accelerating the target as a whole, the light sail mechanism has the potential to produce monoenergetic beams. However, its energy efficiency becomes comparable to that of TNSA only at very high intensities (~10^{22} W/cm^2), where the foil velocity becomes relativistic, introducing a significant Doppler shift in the reflected laser light. The expression for energy per nucleon then takes a form $\varepsilon_p = m_p c^2 \left[\frac{2\xi}{1+2\xi}\right]$, where $\xi = \frac{1}{\rho c^3}$ [84]. Practical challenges in implementing this mechanism include achieving the required target properties and precisely controlling the laser intensity and contrast.

3.3.2. Gas Targets

Thanks to the inverse quadratic dependence of the critical plasma density on the radiation wavelength $\left(n_{cr} \propto \lambda^{-2}\right)$, a solid target used for efficient NIR laser energy deposition can be replaced with an atmospheric density (~10^{19} cm^{-3}) gas when using an LWIR laser. At the vacuum–gas interface, a thin, absorbing super-critical skin layer can be accelerated by the laser's radiation pressure, analogous to the behavior of an ultra-thin foil in the light sail regime.

This interaction leads to a process known as "hole boring" through the plasma [85]. Hole boring occurs when the radiation pressure, $P_{rad} \approx I/c$, surpasses the counteracting thermal pressure from the plasma, $P_{th} = n_e k_B T_e$.

Expressing the laser intensity and electron temperature through a_0, we obtain for linear polarization

$$P_{rad} = n_{cr} m_e c^2 a_0^2 \text{ and } P_{th} = n_e m_e c^2 \left(\sqrt{1 + \frac{a_0^2}{2}} - 1\right).$$

The condition $P_{rad} > P_{th}$ yields the solution $a_0 > \sqrt{\frac{n_e^2}{2n_{cr}^2} - \frac{2n_e}{n_{cr}}}$.

An additional restriction is imposed by the condition of relativistic transparency, at $n_e > \langle\gamma\rangle n_{cr}$. This means that plasma with $n_e > n_{cr}$ could be still under-dense for laser intensities corresponding to $a_0 > \sqrt{\frac{4n_e^2}{n_{cr}^2} - 1}$.

These two "conflicting" conditions for a_0—being high enough to counteract the thermal pressure but below the relativistic transparency regime—define a relatively narrow parameter space for hole boring, as represented by the diagram in Figure 6.

In the cold plasma approximation ($P_{rad} \gg P_{th}$), the critical density layer and the associated electrostatic potential move with a hole-boring velocity $v_{hb} = \sqrt{\frac{(1+R)I}{n_e m_p c}}$, while reflecting plasma ions at twice this velocity ($2v_{hb}$) and imparting them with energy [85]

$$\varepsilon_{hb} = \frac{2(1+R)I}{n_e c}.$$

For the case where $P_{rad} < P_{th}$, the motion of the critical surface is suppressed. However, localized electron heating generates a high-pressure region that expands into the plasma, launching an electrostatic shock propagating at a velocity $v_{sh} = Mc_s$, where M is the Mach number and $c_s = \sqrt{Zk_B T_e/m_p}$ is the ion sound speed [86]. This is termed as a collisionless shock because the thickness of the shock front ($\sim 5\lambda_D$) is much smaller than the collisional mean free path of the particles forming it. At sufficiently high electron temperatures ($T_e \approx 5$ keV), the shock velocity v_{sh} can exceed the hole-boring velocity v_{hb} calculated for a cold plasma.

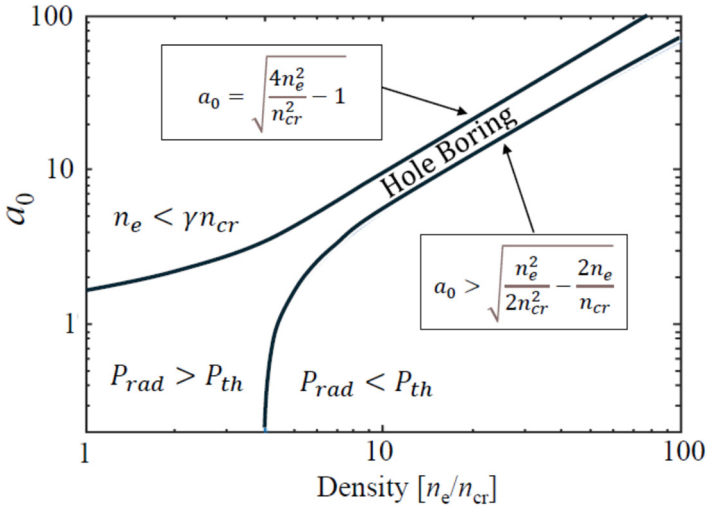

Figure 6. Parameter space for radiation pressure hole boring.

Much like hole-boring acceleration, a sharp particle density shock front and its associated strong electrostatic potential can reflect ions at twice the shock velocity ($2v_{sh}$) corresponding to the energy

$$\varepsilon_{sh} = \frac{Z(1+k)^2 I}{2n_e c},$$

where k is an adiabatic coefficient ($k = 5/3$ for ideal gas) [87]. Such a shock can continue propagating through the plasma even after the laser pulse has terminated, transferring its energy primarily to the ion beam.

Notably, all the RPA regimes exhibit a favorable scaling of ion energy with laser intensity, $\varepsilon_p \sim I$, in contrast to the $\varepsilon_p \sim \sqrt{I}$ scaling characteristic of the TNSA mechanism. This advantageous scaling, coupled with the monoenergetic nature of the ion spectrum, positions RPA as a promising candidate for generating high-energy ion beams required for applications demanding precise control over penetration depth and dosage, such as hadron cancer therapy. Gas jet targets offer additional benefits, including their ability to serve as sources of pure and exotic ion beams, as well as the capability for rapid target replenishment, enabling high repetition rates.

3.3.3. Experimental Results and Prospects

Historically, LWIR lasers combined with gas jet targets were the first to demonstrate both hole boring and shock wave regimes of proton acceleration [88,89]. The most systematic tests of hole boring in gaseous targets have been conducted at ATF through a series of collaborative experiments involving BNL, Imperial College London, Stony Brook University and the Naval Research Laboratory [89–92].

An additional benefit of using LWIR radiation, highlighted in these experiments, is the ability to optically probe plasma interactions using time-resolved interferometry and shadowgraphy [93]. Plasma at the critical density for LWIR radiation remains transparent to visible light, such as the second harmonics of Nd:YAG or TiS lasers. By transversely scanning the laser–plasma interaction region and monitoring optical phase shifts induced by density gradients, plasma density distributions can be inferred. Additionally, splitting the probe beam by polarization and employing independent temporal tuning enabled dual-time optical probing laser–plasma interactions during a given shot. This capability enabled researchers to study plasma dynamics at super-critical density with high temporal and spatial resolution.

An essential requirement for achieving radiation pressure acceleration regimes is the formation of a sharp vacuum–plasma interface with a near-critical density front. This can be performed by using a tailored pre-pulse that arrives several nanoseconds before the main pulse. Such a pre-pulse is typically produced by amplified leakage from the regenerative CO_2 laser amplifier. The pre-pulse generates a blast wave that propagates through the gas jet, with the compressed front of this blast wave serving as a target for the main laser pulse to initiate hole boring through the downstream plasma.

The optimal pre-pulse energy, depending on the initial gas pressure, was found to range between 1 and 5 mJ—approximately 0.1% of the energy in the main pulse. Lower pre-pulse energy was insufficient to form a sufficiently strong blast wave, while higher energy could over-penetrate the gas jet (typically produced with a 1 mm cylindrical nozzle), leaving an empty channel that rendered the main pulse ineffective [91].

Alternatively, an auxiliary Q-switched Nd:YAG laser, focused on the edge of the nozzle, was employed to achieve the same blast wave effect. This method provided easier control over the gas density shaping by allowing independent variation in the timing and energy of the Nd:YAG laser [92]. Additionally, it enabled the exploration of regimes involving the collision of two blast waves, which facilitated the investigation of super-thin critical-density targets (see Figure 7).

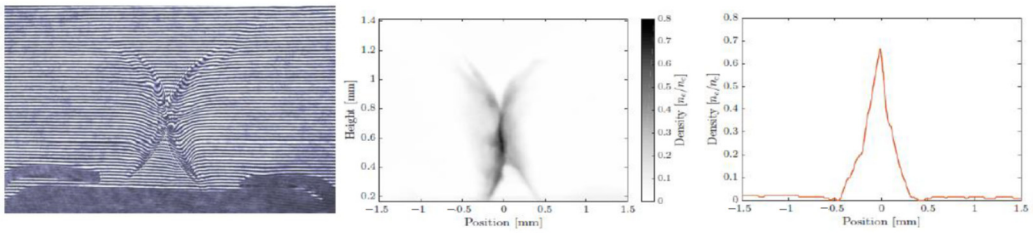

(**a**) (**b**) (**c**)

Figure 7. Interferometry of colliding blast waves (**a**,**b**), its plasma density reconstruction, and (**c**) its density profile taken at the 0.6 mm height over the nozzle edge [94].

A remarkable feature distinguishing the RPA regime from TNSA is the ability to generate monoenergetic ion beams, as has been verified in ATF experiments and illustrated in Figure 8. These sample spectra were obtained from both a foil and a hydrogen gas jet under identical LWIR laser irradiation conditions using a magnetic spectrometer with an entrance pinhole. While the TNSA spectrum exhibits a Maxwellian distribution, the RPA spectrum is sharply defined and limited only by the instrument's acceptance, providing an upper estimate of the proton energy spread at $\Delta\varepsilon_p \leq 4\%$ [90].

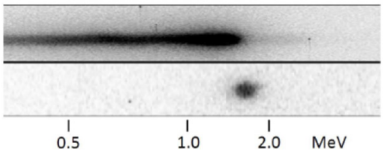

(**a**)

(**b**)

Figure 8. Comparison of (**a**) the TNSA proton spectrum with (**b**) the RPA proton spectrum obtained in ATF experiments with solid and gaseous targets, correspondingly.

Interestingly, under certain conditions, the monoenergetic spectral component of the proton beam exhibited an extremely narrow angular divergence, with a half-opening angle of $\leq 1^\circ$ (see Figure 9). The underlying cause of this phenomenon remains unclear but is hypothesized to result from laser filamentation and hosing instability in relativistically transparent near-critical plasma, leading to narrow yet randomly positioned proton beams. Special profiling of the plasma distribution upstream of the critical layer, such as laser chan-

neling, could prove effective in generating ion beams with controlled angular divergence and energy spread.

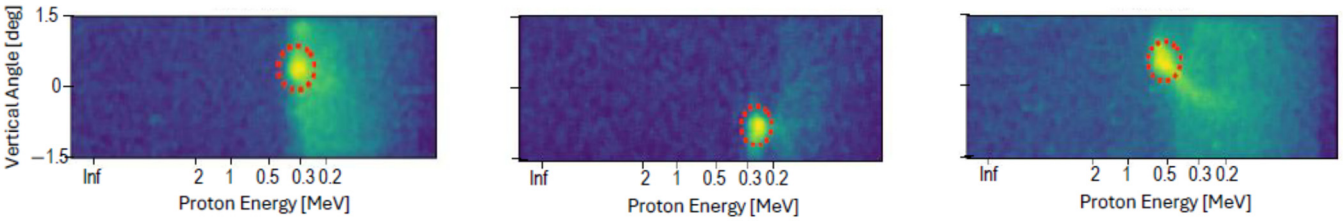

Figure 9. A series of consecutive laser shots reveal a monoenergetic component of the proton beam (along the horizontal scale) together with its narrow angular distribution and its pointing instability visible across the vertical dimension of the spectrometer slit [94].

In addition to visualizing the process of hole boring, optical diagnostics have also been employed for investigations of electron beam instabilities and filamentation phenomena, providing valuable insights into the underlying physics of these processes [92]. Figure 10 illustrates the results of the electron filamentation studies. In this figure, Figure 10b depicts simulated hot electron jets emerging from the laser focus at the vacuum–plasma interface. Figure 10a shows the simulated distribution of cold plasma electrons channeled along the paths of the hot electron jets, while the experimental shadowgraphy in Figure 10c closely matches these simulations shown in Figure 10a.

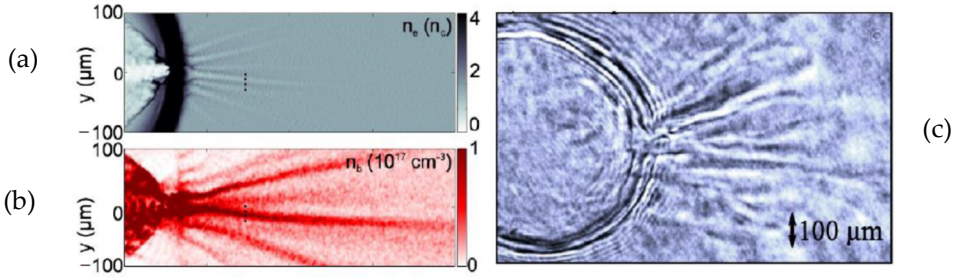

Figure 10. Simulated electron plasma density distribution (**a**) induced by electron filamentation (**b**) compared with experimentally observed shadowgram (**c**) [95].

For most laser shots, the energy of the accelerated protons aligns well with the expected dependence for the hole-boring mechanism. However, some experimental data points significantly exceed these values, fitting an alternative mechanism of the shock wave acceleration, as illustrated in Figure 11. We shall anticipate that shock wave acceleration will become the predominant ion acceleration mechanism as laser intensity increases.

The interaction of the LWIR laser with a critical-density gas target, provides an efficient method for generating pure, impurity-free ion beams, such as protons from hydrogen gas. In a similar manner, we can anticipate obtaining deuterons from deuterium, and ion beams such as $^4He^{2+}$ (alpha particles) and $^3He^{2+}$ ions from ^4He and ^3He gases, respectively. The monoenergetic nature of the resulting ion beams offers significant advantages for applications in nuclear science, such as sharpening the energy distribution in neutron beams produced via nuclear reactions (p,n), (d,n), and (α,n) on light targets like ^9Be or lithium, as well as for injection into conventional ion accelerators.

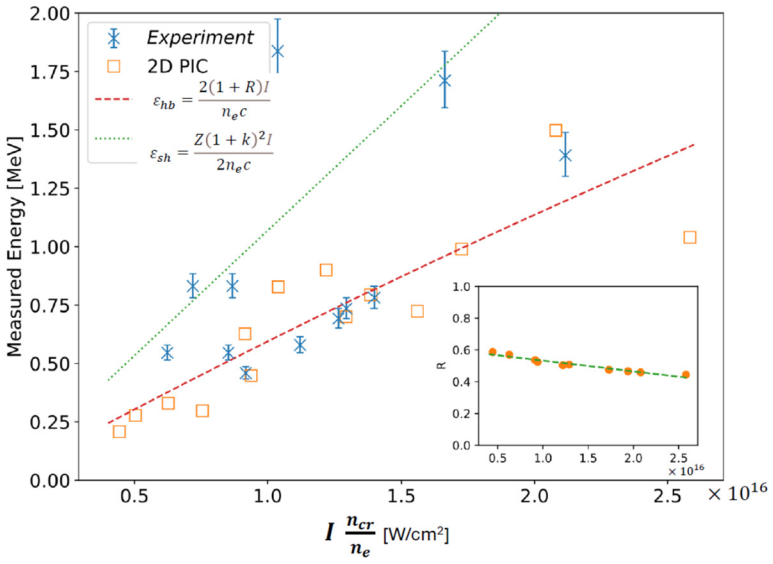

Figure 11. Fitting of experimental proton spectra to hole boring and collisionless shock wave models [94]. The inserted panel presents the simulated reflection.

4. Radiation Sources

4.1. From THz to EUV and Beyond

Several distinctive features of LWIR lasers make them highly attractive for driving secondary radiation sources, spanning a broad spectral range from THz to X-rays (~10^{11}–10^{19} Hz). One notable application involves Q-switched CO_2 gas lasers used to convert tin (Sn) microparticles into radiating plasma for 13.5 nm extreme ultraviolet (EUV) lithography [96].

CO_2 lasers are preferred in this context due to their availability as high-average-power, energy-efficient systems capable of delivering sufficiently short, nanosecond-scale pulses. Notably, LWIR CO_2 laser energy can be efficiently deposited into low-density tin plasma, minimizing EUV reabsorption.

This approach builds on early demonstrations at ATF, which confirmed the effectiveness of nanosecond pulses as an energy-efficient alternative to picosecond LWIR lasers for this application [97].

The advantages of LWIR lasers for enabling secondary radiation sources extend far beyond the EUV lithography. This broader potential was underscored in a 2023 Report on the Basic Research Needs Workshop on Laser Technology [98], saying: "Frequency conversion to either lower or higher photon energies is often greatly enhanced with mid-IR input fields, relative to visible and NIR inputs".

HHG and THz generation are promising applications of LWIR lasers as secondary radiation sources, particularly benefiting from picosecond or, ideally, femtosecond LWIR pulses. A key advantage of LWIR lasers for these applications lies in the well-known scaling $U_p \propto \lambda^2$, which allows LWIR fields to more effectively drive electronic and bipolar responses in materials and gases. This facilitates the efficient generation of deep ultraviolet (UV) and X-ray photon energies, as well as down-conversion to THz frequencies.

The mechanism of HHG in atomic gases relies on the creation of a strong dipole moment between an ionized atom and an electron. The electron is ejected from the atom via potential barrier suppression induced by a strong laser field, and subsequently recollides with the atom during the next half-cycle of the laser [99]. The high-energy cutoff of the harmonics radiated by this dipole, given by $3.2U_p + U_i$, is determined by the atom's first ionization potential (U_i) and the average electron energy upon impact ($3.2U_p$) [100]. The intensity of harmonic generation from an individual dipole is also governed by U_p.

Considering the phase-matching condition necessary for HHG in a neutral gas, the cutoff energy scales as $\lambda^{1.7}$ [99,101], suggesting that HHG supercontinua driven by a CO_2 laser could reach photon energies as high as 10 keV. Such HHG sources hold promise for applications in attosecond X-ray spectroscopy [100]. Progress in this direction hinges on the development of novel high-repetition-rate femtosecond LWIR sources (see Section 2).

A key challenge in extending HHG drivers deeper into the LWIR range is the predicted drop in the energy conversion efficiency, which scales as $\lambda^{-5} - \lambda^{-6}$ [101,102]. Nevertheless, the advantages of long-wavelength laser drivers for HHG have been convincingly demonstrated using a 3.9 μm pump laser [103], spurring interest in experimental demonstrations in the 9–10 μm range accessible with CO_2 lasers.

THz sources are highly desirable for a wide range of applications, from material science to particle acceleration [104,105]. Their non-ionizing nature and ability to penetrate a biological tissue make THz radiation a promising alternative to X-rays for detecting cancerous cells [106,107]. When focused on millimeter-scale spot sizes, THz beams can produce electric fields in the order of GV/m. These intense fields enable the study of structural transitions in polar molecules. Furthermore, the associated transient magnetic fields, reaching the order of a Tesla, can be used to induce magnetic or spin excitations in atoms and molecules and to observe their dynamics on a picosecond timescale.

Currently available high-power THz sources range from large-scale facilities, such as linear accelerators [108], to compact systems based on optical rectification (OR) in nonlinear crystals [109]. Both approaches have their limitations.

Accelerator-based THz sources based on coherent transition radiation (CTR) deliver high peak power (megawatts) and high repetition rates but are large, expensive, and offer limited accessibility. Another active area of accelerator-based research is the generation of narrowband THz FEL radiation using low energy linacs and undulators. These proof-of-principle experiments pave the way for tunable, high-repetition-rate THz sources providing pulses with energies in the millijoule range [110].

Compact OR-based sources, presently driven by NIR lasers, are more economical; however, their yield is constrained by the damage threshold of the nonlinear crystals. The use of LWIR radiation is particularly appealing for OR-based methods due to its low multi-photon absorption in small bandgap semiconductors like GaAs. This characteristic helps reduce crystal damage, thereby increasing THz yields to several millijoules per pulse [111].

In contrast, material damage limitations do not apply to laser-generated plasmas from solid targets. In such cases, THz EM waves emerge as transition radiation, generated when hot electrons propagate through the target crossing the target-vacuum rear boundary.

THz pulses at the 200 mJ level and terawatt scale, emitted from the rear side of the foil, with up to ~0.3% laser-to-THz energy conversion efficiency, have been demonstrated at picosecond NIR laser facilities [112], using setups identical to those employed for the TNSA method of laser-driven ion acceleration. The intensity of this radiation is quadratically proportional to the total electric charge carried by hot electrons. Consequently, the high efficiency of LWIR lasers in generating hot electrons, as highlighted in Section 3.3, could prove equally advantageous for THz production in this regime. This promising potential has yet to be experimentally verified.

4.2. Inverse Compton Scattering

We now shift our focus to X-ray sources based on inverse Compton scattering (ICS), a process that involves the interaction of electron and laser beams. This approach has been extensively studied at ATF, leveraging the facility's access to lasers and an electron linac.

Passing through the laser focus, relativistic electrons with velocity $v = \beta c$, where β is the relativistic factor, scatter laser photons within a narrow-divergence cone of

a half-opening angle $\theta_0 = {}^1/_\gamma$, centered along the electron beam propagation, where $\gamma \equiv \frac{1}{\sqrt{1-\beta^2}} = \varepsilon_e[\text{MeV}]/0.511$ is the Lorentz factor. The scattered photons emerge Doppler-shifted to the wavelength

$$\lambda_\gamma \approx \frac{\lambda}{4\gamma^2}\left(1 + a_0^2 + \gamma^2\theta^2 + \phi^2/4\right),$$

where θ is the observation angle and ϕ is the collision angle [113]. In the case of a counter-propagation geometry, $\phi = 0$, we obtain the shortest wavelength of scattered X-rays and the best efficiency of the laser/e-beam interaction.

To estimate the total number of scattered photons (N_γ) under realistic experimental conditions—where electron bunch containing N_e electrons matches the cross-section of the laser focus, and the laser/e-beam interaction length is limited by the Rayleigh range of the laser focus, $Z_R = \pi w_0^2/\lambda$—we use the following formula:

$$N_\gamma \cong \sigma_T N_e n_L Z_R,$$

where σ_T = 6.65 × 10^{-17} μm^2 is the Thomson cross-section, and n_L is the number density of laser photons.

4.2.1. ATF Experiments

An LWIR laser delivers an order-of-magnitude higher number of photons per joule of energy compared to NIR lasers. This advantage supports the expectation of high quantum yields in ICS. For the ATF's LWIR laser focused to $w_0 \approx 20$ μm, we estimate $n_L \approx 2 \times 10^{25}$ photons/cm^3 and $Z_R \approx 140$ μm. For 1 nC ($N_e = 6 \times 10^9$) picosecond electron bunches typically provided by the ATF linac and focused to a size compatible with the laser focus, the ICS X-ray yield is estimated to reach 2×10^9 photons per shot [114]. These high yields allow for single-shot imaging of X-ray fluxes using high-resolution microchannel plates, facilitating a broad range of applied ICS studies.

One such application is single-shot phase-contrast tomography, which also benefits from the spatial coherence of the ICS X-ray beam radiated by an electron beam with a small cross-section (~10 μm). This method offers significantly higher image resolution compared to traditional absorption-based techniques.

Single-shot tomography is particularly suitable for time-resolved imaging of fast processes or for examining delicate objects that evolve under prolonged irradiation. To achieve this, the method requires short X-ray fluxes sufficient to record images in a single-shot exposure.

The ability to retrieve phase information from single-shot images of material and biological test objects using ICS sources was first demonstrated in ATF experiments [115,116]. These experiments utilized 10 keV picosecond ICS X-rays generated by the interaction of a CO_2 laser beam with 80 MeV electron bunches.

In contrast, systems employing NIR lasers typically require multi-shot exposures to achieve similar results.

Notably, in the focused ATF LWIR laser beam, the parameter a_0 can reach and exceed unity, signifying that the laser field is sufficiently strong to drive oscillating electrons into a regime of relativistic transverse motion. In this regime, the transverse oscillations become non-sinusoidal, and the Lorentz force arising from the laser's magnetic fields induces a nonlinear figure-eight electron motion in the relativistic frame. This motion gives rise to three significant effects:

First, the direct propagation of electrons slows down as they are redirected into transverse oscillations. This phenomenon can also be described as an effective mass increase, $m_{e,eff} \equiv \langle\gamma\rangle m_e$, which results in redshift in the radiated spectrum.

Second, the nonlinear motion introduces harmonic components into the radiated spectrum, enriching its complexity and expanding its frequency range.

Finally, the nonlinear transverse motion imparts distinctive signatures in the angular radiation spectrum, particularly within the harmonics, allowing for their spatial discrimination.

The scaling of a_0 with λ, enabled by the use of LWIR lasers, facilitates access to the nonlinear ICS regime. This regime was rarely explored experimentally before ATF experiments, which successfully achieved single-shot visualization of the characteristic intensity distribution of second and third harmonics, along with a redshift consistent with theoretical predictions [117,118].

4.2.2. Possible Light Sources Based on LWIR Lasers

A laser EM field can be conceptualized as a virtual undulator, offering key advantages of synchrotron light sources (SLSs), such as directionality and monochromaticity. ICS sources extend these capabilities by enabling access to hard X-ray and gamma spectral ranges, surpassing the reach of contemporary SLSs. This enhancement is possible because the laser wavelength is orders of magnitude shorter than the period used in conventional magnetic wiggler arrays of SLSs, leading to a significant increase in the frequency of relativistic electron oscillations. Furthermore, the ICS process requires much less energetic electrons to achieve the X-ray range covered by SLSs, paving the way for the development of relatively compact and cost-effective X-ray sources.

Building on proof-of-principle demonstrations [119], the concept of dedicated ICS sources has been realized in practical applications. Examples include the Lyncean Compact Light Source [120], a commercial system operating in the soft X-ray range, as well as gamma-ray sources under development, such as those at the High Energy Accelerator Research Organization (KEK) [121] and Extreme Light Infrastructure Nuclear Physics (ELI-NP) [122]. At the same time, several proposals have been made to adapt existing or newly constructed electron accelerators into high-power ICS sources [123,124].

Most of these ICS projects combine electron beams with pulses from mode-locked, NIR, solid-state lasers. These lasers can operate at multi-megahertz repetition rates, synchronized with RF electron beam sources such as synchrotrons and superconducting energy recovery linacs (SERLs).

Although mode-locked quasi-continuous-wave (quasi-CW) lasers typically have relatively low average power, around 100 W, their potential for driving intense ICS can be significantly enhanced by employing high-finesse Fabry–Perot cavities. These field-enhancement cavities (FECs), tuned to resonate with the laser repetition rate, can accumulate multi-kilowatt average laser power distributed across short picosecond pulses circulating inside the cavity.

When synchronized with counter-propagating electron bunches from high-current accelerators, these laser beams could achieve time-averaged ICS X-ray fluxes of approximately 10^{12} photons per second—over a million times greater than conventional X-ray tubes. This capability positions ICS sources as complementary tools to synchrotron light sources (SLSs) for applications such as structural studies of materials and biological systems, while extending their reach to harder X-rays.

The dual-wavelength combination of laser and X-rays available with pulsed ICS sources presents an attractive opportunity for pump–probe studies. Achieving this requires intense X-ray flashes to produce meaningful datasets from a single pulse. However, the en-

ergy per laser pulse circulating inside an FEC, currently limited to 0.1–1 mJ, restricts single-shot X-ray yields from such ICS sources to a few thousand photons per pulse—insufficient for most pump–probe applications. Increasing the X-ray yield at a given accelerator current would require significantly more laser photons per pulse than current NIR FEC technology can provide. To address this limitation, an approach leveraging state-of-the-art short-pulse LWIR lasers has been proposed [36].

Joule-class pulsed CO_2 lasers can deliver a significantly greater number of photons into the laser–e-beam interaction region, generating picosecond X-ray fluxes that exceed those of NIR-FEC-based ICS sources by several orders of magnitude. This high flux enables single-shot, ultrafast imaging, making CO_2 laser-based ICS sources an optimal choice for studying dynamic processes at the temporal and energy scales of phase transitions, chemical reactions, and molecular interactions.

To achieve an ICS source with high average power and brightness, the laser must operate at a high repetition rate. Commercially available small-aperture (up to 22 mm) high-pressure CO_2 gas lasers can operate at repetition rates of up to 300 Hz, while an inter-electrode distance of approximately 50 mm is also achievable using current high-voltage pulse-forming network technology. By employing pulse-burst mode to multiply the repetition rate, an effective rate exceeding 10 kHz can be achieved [36]. Although this remains orders of magnitude lower than the multi-MHz repetition rates of RF accelerators and mode-locked solid-state lasers, the significantly higher pulse energy achievable with CO_2 lasers, coupled with a greater photon yield per unit of laser energy, allows these systems to achieve average X-ray photon intensities comparable to quasi-CW NIR FEC-based approaches. This has been demonstrated by comparing earlier proposed ICS light sources—based on electron accelerators at Cornell and Frascati driven by NIR lasers [123,124]—with those utilizing a CO_2 laser driver [36].

X-ray brightness is typically the primary parameter used to characterize and compare different light sources. Therefore, it is instructive to evaluate existing and emerging light sources based on this metric, as illustrated in Figure 12.

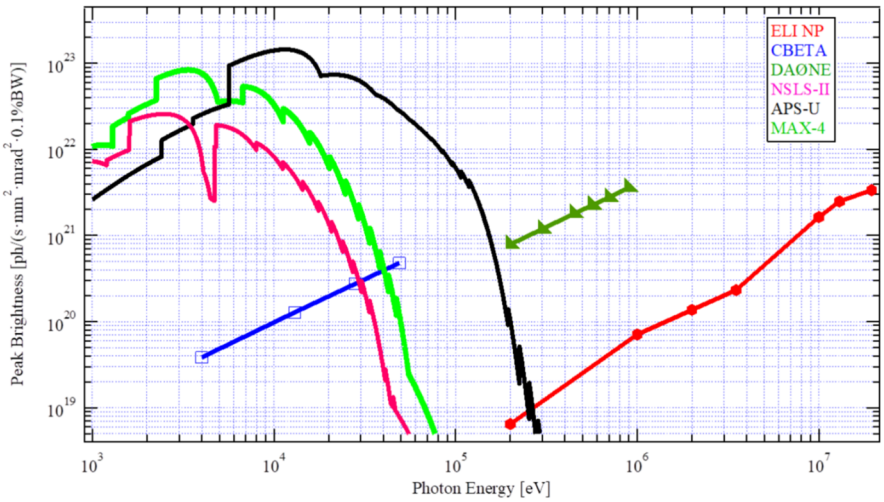

Figure 12. Comparison of ICS sources based on CBETA and DAΦNE electron accelerators with third-generation SLSs and ELI-NP [36].

Similar arguments apply to predicting the performance of ICS sources driven by high-power kHz-class NIR laser systems, whose parameters are comparable to those proposed for high-repetition-rate CO_2 lasers. Consequently, we can anticipate shifting the ICS spectrum to approximately ten-times-higher energies, albeit with roughly an order of magnitude smaller brightness.

Overall, the utility of X-ray and gamma radiation is highly application-dependent, with the photon energy requirements spanning several decades. This breadth cannot be fulfilled by a single source. Consequently, a diverse array of ICS sources—integrating the capabilities of both ring-based and linac-based systems, along with various laser drivers—will be essential to deliver the wide range of characteristics needed to meet current user demands and future challenges.

4.2.3. Electron–Positron and Gamma Colliders

The relevance of LWIR lasers to future plasma-based e^-e^+ colliders goes beyond their role as a practical research tool for exploring low-plasma density LWFA regimes, as discussed in Section 3.1. In addition, LWIR lasers could be considered for lepton-to-gamma converters in both e^-e^+ and gamma–gamma ($\gamma\gamma$) colliders, independent of the particle accelerator technology employed.

Developing a positron injector is one of the most challenging tasks for realizing the next generation e^-e^+ collider. For example, the International Linear Collider (ILC) design specifies a 3-nC charge per positron bunch. Intense beams of circularly polarized gamma rays in the ~30 MeV energy range are needed to produce polarized positrons via bremsstrahlung on a high-Z solid target, with an expected efficiency of converting polarized photons into polarized positrons of about 2% [125]. Consequently, for each positron, 50 gamma photons are required as precursors. The ICS method, utilizing backscattering of a high-intensity 10 μm laser beam off a 4 GeV e-beam, is one of the proposed schemes for such a positron source [126]. This could be achieved via ICS at ten consecutive IPs, where a 4 GeV e-beam, carrying 15 nC charge per bunch, undergoes a head-on collision with a 2 J, several-picosecond LWIR laser pulse to produce one photon per electron ($N_\gamma/N_e = 1$). In comparison, a 20 Joule 1 μm laser pared to a 1.3 GeV e-beam would be required to achieve the same condition. Simultaneously, this would increase the fraction of electron energy lost in each scattering event and make it more difficult to maintain a small e-beam size over multiple IPs due to inherently bigger geometrical emittance of an electron beam of a smaller energy. These considerations suggest that the CO_2 laser could be the optimal driver for the ICS-based polarized positron source [126].

Lepton linear colliders can be readily converted into photon colliders through the ICS process. This offers an opportunity to study lepton-γ and $\gamma\gamma$ interactions at comparable energies and luminosities, alongside e^-e^+ collisions. The $\gamma\gamma$ collider is regarded as a valuable extension of a lepton collider, as it facilitates the direct production of Higgs bosons and provides high cross-sections for pair production of new supersymmetric particles.

Furthermore, if a dedicated stand-alone $\gamma\gamma$ collider were ever considered, its potential technical advantages come to play. These advantages include the elimination of the need for a more complex positron accelerator, as two electron beams would suffice, and the potential to utilize a more energy-efficient, higher-luminosity, low-density LWFA regime. As discussed in Section 3.2, CO_2 lasers could be valuable in this context. Once the beam-strahlung limitation on the maximum bunch charge is no longer a constraint, the scaling of the bunch particle number with plasma density ($N_e \propto 1/\sqrt{n_e}$) can be fully exploited. Given that collider luminosity $\mathcal{L} \propto N_e^2$, this opens up the possibility to reduce the repetition rate ($f \propto n_e$), as well as the electron beam power and the total average laser power ($\propto\sqrt{n_e}$).

As demonstrated by the examples in Table 1, the increase in acceleration per stage at reduced plasma density leads to higher energy requirements for lasers driving each individual stage. This trend is particularly demanding for NIR lasers in low-density regimes ($n_e \leq 3 \times 10^{16}$ cm^{-3}), which require multi-PW peak power and multi-kJ pulse energy. In contrast, mid-IR CO_2 laser parameters appear more practical and achievable, providing

just tens of TW peak power and tens of joules of pulse energy to generate electron bunches with the same charge.

A specific limitation for gamma colliders is imposed by the re-scattering of Compton photons by the laser beam into e^-e^+ pairs. This occurs when the product of the laser photon energy, $\hbar\omega$, and the gamma energy, $\hbar\omega_\gamma$, exceeds the square of the electron rest energy, i.e., when $\omega\omega_\gamma > m^2c^4/\hbar^2$. Based on this condition, the optimum laser wavelength can be derived as $\lambda[\mu\text{m}] = 4.2\varepsilon_e[\text{TeV}]$. For λ = 10 μm, this corresponds to ε_e = 2.4 TeV. This shows that an LWIR laser is much more effective in suppressing parasitic re-scattering in a prospective collider compared to an NIR laser.

It is important to note that for both ICS applications considered for future colliders, a ~1 TW picosecond LWIR laser will be required. This is within current technical capabilities, with the main challenge being an improvement in the repetition rate.

5. Directed Energy

5.1. Mega-Filaments

Up until now, we have focused on processes involving LWIR laser beams converging in a vacuum onto a material, plasma, or electron beam. Now, let us consider a simpler scenario: a powerful laser beam propagating through air. At high laser intensities, the nonlinear component of the refractive index in air, n_2, causes the Kerr effect—positive lensing, which counteracts the beam's natural diffraction. These two competing effects—focusing and divergence—reach equilibrium at the critical power $P_{cr} = 3.77\lambda^2/8\pi n_0 n_2$, where n_0 is the linear optical refractive index. When $P > P_{cr}$, the beam undergoes self-focusing. The beam collapse is prevented by the defocusing effect of plasma generated by a combination of multiphoton, tunneling, and avalanche ionization of molecules in air. The generated plasma introduces a negative contribution to the refractive index, leading to defocusing of the laser. A dynamic competition between these opposing focusing and defocusing effects is established, allowing the beam to remain confined over long distances, significantly exceeding the Rayleigh range [127].

Due to the negligible variations in the refractive indices of air across the NIR and LWIR spectral ranges, the $P_{cr} \propto \lambda^2$ dependence holds. This results in a critical power ranging from $P_{cr} \approx 10$ GW at λ = 1 μm to $P_{cr} \approx 1$ TW at λ = 10 μm. While this may seem attractive for short-wavelength radiation, it becomes a disadvantage at higher intensities ($P \gg P_{cr}$), where a single beam breaks into multiple filaments that fan out from the original beam propagation, with each filament carrying a power of $P \approx P_{cr}$. This small-scale filamentation [128] is triggered by intensity fluctuations in the beam profile, which are amplified by modulational instability. As a result, a higher P_{cr} allows LWIR beams to transport significantly higher energy in a well-collimated manner compared to NIR beams.

It has been predicted that beam parameters also scale with λ, causing a single filament to extend from tens of meters in length and ~100 μm in diameter at NIR wavelengths to approximately 1 km and 1 cm, correspondingly, at LWIR wavelengths.

Additionally, Earth's atmospheric transmittance favors certain spectral windows with low molecular absorption. Among these, the LWIR atmospheric window between 8 and 14 μm offers the smallest molecular and aerosol scattering.

Laser filamentation in air has been extensively studied in the NIR spectral range, where most intense ultrafast lasers operate [129]. However, only recently have the first experimental validations of the LWIR filamentation regime been conducted [130–132]. In recent ATF experiments [131,132], researchers employed laser pulses with a duration of 3.5 ps and ≥1 TW peak power at a central wavelength of 10.2 μm. These experiments revealed the formation of a single centimeter-diameter filament in air, capable of carrying

several joules of energy over a distance of 32 m (~$20Z_R$), constrained only by the available laboratory space.

5.2. Applications

Long-distance, single-filament laser beam propagation is significant not only for energy transport and the potential creation of extended ionized channels for lightning mitigation but also for many other applications relevant to the field of directed energy research. These include remote atmospheric probing, detection of radioactive sources, and radiofrequency (RF) EM pulse generation. Two such opportunities have been explored at ATF and are discussed in this section. In both cases, the benefits of wavelength scaling, as highlighted earlier in the context of ionization and electron heating processes, are evident once again.

Long-range stand-off detection of radioactive materials is an application of significant interest to various communities, including national defense and disaster response. The ATF's LWIR laser enables the exploration of a novel detection method that leverages a laser-driven electron avalanche, initiated by air ionization in the vicinity of a radioactive source [133]. The method is aimed at high-sensitivity detection of ionizing sources that produce ultra-low concentrations of electrons and negative ions—down to one part in 10^{16}. In this context, even a very low ionization rate of neutral air by the laser could seed spontaneous avalanches, potentially obscuring the desired diagnostic signals.

The use of an LWIR laser ensures high detection sensitivity by offering two important advantages:

First, the small photon energy of LWIR lasers significantly reduces ionization probabilities compared to NIR lasers. For example, at 1 TW/cm^2, the probability of multiphoton ionization of oxygen at λ = 9.2 μm is approximately 10^{23} times lower than at λ = 1 μm, thereby greatly enhancing the selectivity and sensitivity of this diagnostic technique.

Second, the electron heating rate scales with $I_L\lambda^2$, enabling more efficient avalanche generation at longer wavelengths.

Figure 13 illustrates this capability, showing an LWIR laser filament collapsing into a bright spark of super-critical plasma upon entering a region pre-ionized by alpha radiation from a Po-210 source with milli-Curie-level intensity [134]. The joule-level energy of LWIR pulses, with picosecond durations, might be sufficient to induce detectable avalanches up to a kilometer away [135].

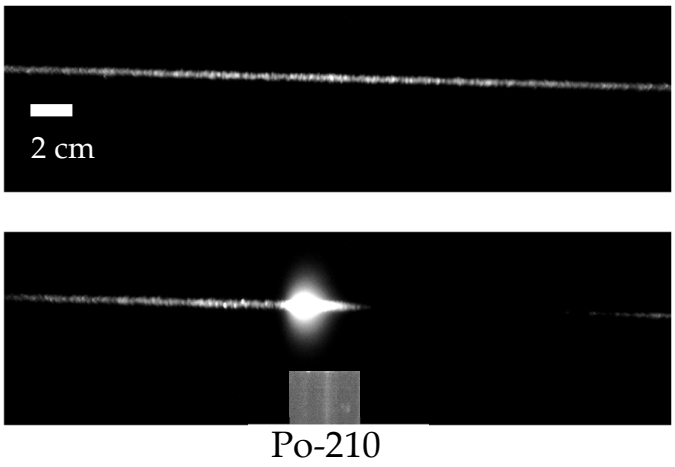

Figure 13. Detection of a radioactive source in the ATF user experiment [134].

Secondary radiation from laser-driven plasma filaments offers access to the microwave spectral range. For these radiation fields to emerge, plasma currents must act as radiating

sources. Two primary contributors to these currents are the bulk plasma current and the plasma surface wake current, both of which are driven by the ponderomotive force of the laser field. These currents propagate at the speed of light behind the laser pulse, generating a cone of radially polarized, broadband microwave electromagnetic waves. The strongest emission lobe has an opening angle of $\theta \approx \sqrt{\lambda_{RF}/L}$, where λ_{RF} is the wavelength of the detected RF signal and L is the plasma column length.

The magnitude of these currents and the resulting radiation strength scale strongly with the laser wavelength due to their ponderomotive origin [136]. This scaling was experimentally verified at ATF, where a 9.2 μm laser demonstrated a laser-to-RF energy conversion efficiency approximately 300 times higher than a 1 μm laser with similar parameters [137]. Figure 14 illustrates this outcome. Note that the RF intensity is quadratic to the measured RF field amplitude shown in the plots of Figure 14.

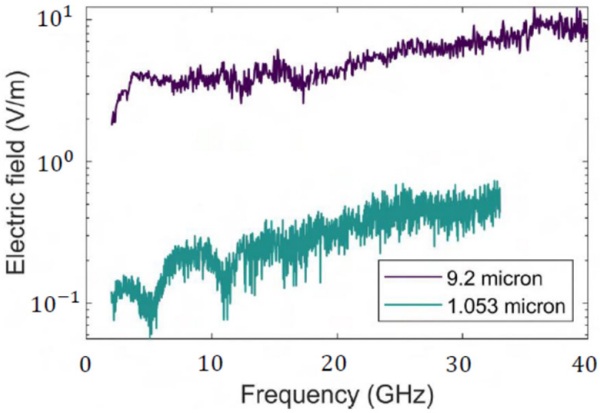

Figure 14. Comparison between detected field amplitudes within the 2-33 GHz spectral range produced by NIR and LWIR laser-driven plasma filaments [137].

Measuring the microwave radiation provides valuable insight into the internal dynamics of the plasma channel. On a practical note, the ponderomotive currents in air plasmas may serve as useful sources of microwave radiation for ultrabroadband, single-shot, and pump–probe spectroscopy. This could enable the measurement of material properties in the RF spectrum on a picosecond timescale, which has traditionally been difficult to access but is becoming increasingly significant in technological applications.

6. Conclusions

Until recently, the performance of pulsed LWIR lasers was comparable to that of high-peak-power NIR lasers from the early 1990s, prior to the development of the chirped pulse amplification (CPA) technique [4]. Since the advent of CPA, ultrafast NIR lasers have driven significant progress in plasma-based accelerator research. The recent incorporation of the CPA method into gas laser technology [2,16] positions LWIR lasers to become a valuable complement to NIR lasers, opening new avenues for future breakthroughs in the field.

The primary goal of this paper is to raise awareness within the scientific community working in advanced accelerators and radiation sources about the unique capabilities of LWIR lasers in addressing critical challenges outlined in recent guiding reports. Notably, the 2023 Basic Research Needs Workshop on Laser Technology [98] emphasizes the need for mid-IR lasers, while the P5 Panel 2024 Report [70] underscores the importance of test facilities for future particle accelerators.

This review reflects the authors' insight into the development of ultrafast LWIR laser technology and its transformative applications in user experiments conducted at the BNL

ATF over the past two decades. We have highlighted the advantages of LWIR lasers through various examples, focusing on the favorable wavelength scaling of key physical phenomena fundamental to laser-matter interactions. These attributes include ponderomotive electron heating, avalanche ionization, critical plasma density thresholds, and increased photon yield per unit of laser energy. This positions ultrafast, high-peak-power LWIR lasers as promising and versatile tools for strong-field applications.

Potential applications include compact particle sources via laser-driven plasma acceleration, X-ray ICS sources, electron-to-gamma conversion for colliders, EM energy transport through the atmosphere for remote interrogation of nuclear materials, and the generation of intense THz and GHz waves.

ATF's picosecond CPA LWIR laser represents a cutting-edge advancement in high-peak-power gas laser technology. As efforts to compress its pulses to femtosecond durations progress, new transformative applications are expected to emerge, further propelling accelerator science and unlocking new frontiers in related fields.

The examples highlighted in this review represent a limited selection from the broader range of notable experimental achievements made with the ATF's CO_2 laser over the past three decades, including the following:

- **Inverse Cherenkov Electron Acceleration**: Relativistic electron acceleration in gas using radially polarized LWIR laser beams [138], laying the groundwork for direct electron acceleration in a vacuum [139] and enabling the generation of strong longitudinal magnetic fields when converting to azimuthally polarized beams [140].
- **First Staged Laser Accelerator**: The STELLA experiment demonstrated the first two-stage, monoenergetic Inverse Free Electron Laser (IFEL) accelerator [141].
- **High Gain Harmonic Generation (HGHG)**: The pioneering FEL method is now widely used in accelerator facilities globally [142].
- **Multiple Innovations in IFEL Technique**: Achievements include monoenergetic electron acceleration using helical undulators (RUBICON experiment) [143], high-duty-cycle IFEL operation with bursts of electron bunches interacting with laser pulses circulating through a laser amplifier [144] and boosting the ICS photon energy by integrating the ICS process at the output of the IFEL accelerator [145].

These accomplishments underscore the unique synergy between the LWIR laser and the high-brightness photocathode RF electron linac—a hallmark of the ATF—making it a one-of-a-kind facility to drive innovation in advanced accelerators and radiation sources.

As a proposal-driven DOE Office of Science National User Facility, ATF provides access to a broad scientific community interested in pursuing innovative research that leverages its unique capabilities.

Author Contributions: Conceptualization, I.V.P. and M.N.P.; methodology, I.V.P. and M.N.P.; software, M.N.P.; validation, I.V.P. and M.N.P.; formal analysis, I.V.P.; investigation, I.V.P.; resources, M.N.P.; data curation, M.N.P.; writing—original draft preparation, I.V.P.; writing—review and editing, I.V.P. and M.N.P.; visualization, I.V.P. and M.N.P.; supervision, I.V.P.; project administration, I.V.P.; funding acquisition, I.V.P. All authors have read and agreed to the published version of the manuscript.

Funding: This research was funded by the U.S. Department of Energy under contract DESC0012704.

Institutional Review Board Statement: Not applicable.

Informed Consent Statement: Not applicable.

Data Availability Statement: No original data have been generated in the course of this study.

Conflicts of Interest: The authors declare no conflicts of interest. The funders had no role in the design of the study; in the collection, analyses, or interpretation of data; in the writing of the manuscript; or in the decision to publish the results.

Abbreviations

The following abbreviations are used in this manuscript:

ATF	Accelerator Test Facility
BNL	Directory of open access journals
CW	Continuous wave
DC	Dispersive compression
CPA	Chirped pulse amplification
CTR	Coherent transition radiation
DOE	U.S. Department of Energy
ELI-NP	Extreme Light Infrastructure—Nuclear Physics
EM	Electromagnetic
EUV	Extreme ultraviolet
FEC	Field-enhancement cavity
FEL	Free electron laser
GVD	Group velocity dispersion
HHG	High-harmonic generation
ICS	Inverse Compton scattering
IFEL	Inverse free electron laser
IP	Interaction point
LHC	Large Hadron Collider
LWFA	Laser wakefield acceleration
LWIR	Long wave infrared
NIR	Near-infrared
OPO	Optical parametric oscillator
OPCPA	Optical parametric chirped pulse amplification
OR	Optical rectification
RF	Radiofrequency
RPA	Radiation pressure acceleration
RSF	Relativistic self-focusing
SLS	Synchrotron light source
SM	Self-modulated
SPM	Self-phase modulation
TNSA	Target normal sheath acceleration
UCLA	University of California in Los Angeles

References

1. Haberberger, D.; Tochitsky, S.; Joshi, C. Fifteen terawatt picosecond CO_2 laser system. *Opt. Express* **2010**, *18*, 17865–17875. [CrossRef] [PubMed]
2. Polyanskiy, M.N.; Pogorelsky, I.V.; Babzien, M.; Kupfer, R.; Vafaei-Najafabadi, N.; Palmer, M.A. High-peak-power long-wave infrared lasers with CO_2 amplifiers. *Photonics* **2021**, *8*, 101. [CrossRef]
3. BNL Accelerator Test Facility. Home Page. Available online: www.bnl.gov/atf/.
4. Strickland, D.; Mourou, G. Compression of amplified chirped optical pulses. *Opt. Commun.* **1985**, *56*, 219–221. [CrossRef]
5. Yang, Y.; Lee, J.; Wang, J. Energetic picosecond 10.2-μm pulses generated in a BGGSe crystal for nonlinear seeding of terawatt-class CO2 amplifiers. *Opt. Express* **2024**, *32*, 11182–11192. [CrossRef]
6. Yin, Y.; Chew, A.; Ren, X.; Li, J.; Wang, Y.; Wu, Y.; Chang, Z. Towards Terawatt sub-cycle long-wave infrared pulses via chirped optical parametric amplification and indirect pulse shaping. *Sci. Rep.* **2017**, *7*, 45794. [CrossRef]
7. Chang, Z.; Fang, L.; Fedorov, V.; Geiger, C.; Ghimire, S.; Heide, C.; Ishii, N.; Itatani, J.; Joshi, C.; Kobayashi, Y.; et al. Intense infrared lasers for strong-field science. *Adv. Opt. Photonics* **2022**, *14*, 652–782. [CrossRef]
8. Kast, S.J.; Schwarzschild, B.M. Performance comparison of pulsed discharge and E-beam controlled CO_2 lasers. *J. Appl. Phys.* **1973**, *44*, 1631–1637. [CrossRef]
9. Goldstone, P.D.; Allen, G.; Jansen, H.; Saxman, A.; Singer, S.; Thuot, M. The Antares Facility for Inertial Fusion Experiments—Status and Plans. In *Laser Interaction and Related Plasma Phenomena*; Hora, H., Miley, G.H., Eds.; Springer: Boston, MA, USA, 1984. [CrossRef]

10. Jie Ma, J.; Qin, Z.; Xie, G.; Qian, L.; Tang, D. Review of mid-infrared mode-locked laser sources in the 2.0 μm–3.5 μm spectral region. *Appl. Phys. Rev.* **2019**, *6*, 021317. [CrossRef]
11. Alcock, A.; Corkum, P. Ultra-fast switching of infrared radiation by laser-produced carriers in semiconductors. *Can. J. Phys.* **1979**, *57*, 1280–1290. [CrossRef]
12. Alcock, A.J.; Leopold, K.; Richardson, M.C. Continuously tunable high-pressure CO_2 laser with uv photopreionization. *Appl. Phys. Lett.* **1973**, *23*, 562–564. [CrossRef]
13. Shimada, T.; Bigio, I.J.; Kurnit, N.A.; Harrison, R.F. Large-volume high-pressure CO_2 laser for ultrashort pulse amplification. In Proceedings of the 1988 Conference on Lasers and Electro-Optics, OSA Technical Digest, Anaheim, CA, USA, 25–29 April 1988; Volume 7, p. FD2.
14. Polyanskiy, M.N.; Pogorelsky, I.V.; Babzien, M.; Kupfer, R.; Palmer, M.A. Ultrashort-pulse, terawatt, long-wave infrared lasers based on high-pressure CO_2 amplifiers. *EPJ Web Conf.* **2021**, *255*, 11010. [CrossRef]
15. Polyanskiy, M.N.; Pogorelsky, I.V.; Yakimenko, V. Picosecond pulse amplification in isotopic CO_2 active medium. *Opt. Express* **2011**, *19*, 7717–7725. [CrossRef]
16. Polyanskiy, M.N.; Pogorelsky, I.V.; Babzien, M.; Palmer, M.A. Demonstration of a 2 ps, 5 TW peak power, long-wave infrared laser based on chirped-pulse amplification with mixed isotope CO_2 amplifiers. *OSA Contin.* **2020**, *3*, 459–472. [CrossRef]
17. Polyanskiy, M.N.; Pogorelsky, I.V.; Babzien, M.; Kupfer, R.; Li, W.; Palmer, M.A. 9.3 Microns: Toward a next-generation CO2 laser. In Proceedings of the 2022 IEEE Advanced Accelerator Concepts Workshop (AAC), Long Island, NY, USA, 6–11 November 2022; pp. 1–4. [CrossRef]
18. Polyanskiy, M.N.; Pogorelsky, I.V.; Babzien, M.; Li, W.H.; Kupfer, R.; Palmer, M.A. Multi-terawatt, sub-picosecond long-wave infrared laser for next-generation article accelerators. In Proceedings of the 14th International Particle Accelerator Conference, Venice, Italy, 7–12 May 2023. [CrossRef]
19. Pogorelsky, I.V.; Polyanskiy, M.N.; Kimura, W.D. Mid-infrared lasers for energy frontier plasma accelerators. *Phys. Rev. Acc. Beams* **2016**, *19*, 091001. [CrossRef]
20. Kupfer, R.; Wang, F.; Wishart, J.F.; Babzien, M.; Polyanskiy, M.N.; Pogorelsky, I.V.; Rao, T.; Cultrera, L.; Vafaei-Najafabadi, N.; Palmer, M.A. Raman wavelength conversion in ionic liquids. *Phys. Rev. Appl.* **2023**, *19*, 014052. [CrossRef]
21. Qu, S.; Liang, H.; Liu, K.; Zou, X.; Li, W.; Wang, Q.J.; Zhang, Y. 9 μm few-cycle optical parametric chirped-pulse amplifier based on $LiGaS_2$. *Opt. Lett.* **2019**, *44*, 2422–2425. [CrossRef] [PubMed]
22. Corkum, P. Amplification of picosecond 10 μm pulses in multi-atmosphere CO_2 lasers. *IEEE J. Quan. Electron.* **1985**, *21*, 216–232. [CrossRef]
23. Gustafson, T.; Kelley, P.; Fisher, R. Subpicosecond pulse generation using the optical Kerr effect. *IEEE J. Quan. Electron.* **1969**, *5*, 325. [CrossRef]
24. Voronin, A.A.; Zheltikov, A.M.; Ditmire, T.; Rus, B.; Korn, G. Subexawatt few-cycle lightwave generation via multipetawatt pulse compression. *Opt. Commun.* **2013**, *291*, 299–303. [CrossRef]
25. Hädrich, S.; Kienel, M.; Müller, M.; Klenke, A.; Rothhardt, J.; Klas, R.; Gottschall, T.; Eidam, T.; Drozdy, A.; Jójárt, P.; et al. Energetic sub-2-cycle laser with 216W average power. *Opt. Lett.* **2016**, *41*, 4332–4335. [CrossRef]
26. Hemmer, M.; Baudisch, M.; Thai, A.; Couairon, A.; Biegert, J. Self-compression to sub-3-cycle duration of mid-infrared optical pulses in dielectrics. *Opt. Express* **2013**, *21*, 28095–28102. [CrossRef]
27. Shumakova, V.; Malevich, P.; Ališauskas, S.; Voronin, A.; Zheltikov, A.M.; Faccio, D.; Kartashov, D.; Baltuška, A.; Pugžlys, A. Multi-millijoule few-cycle mid-infrared pulses through nonlinear selfcompression in bulk. *Nat. Commun.* **2016**, *13*, 12877. [CrossRef]
28. Bravy, B.G.; Gordienko, V.M.; Platonenko, V.T. Self-compression of terawatt level picosecond 10 μm laser pulses in NaCl. *Laser Phys. Lett.* **2014**, *11*, 065401. [CrossRef]
29. Pigeon, J.; Tochitsky, S.; Joshi, C. Generation of high power, sub-picosecond, 10 μm pulses via self-phase modulation followed by compression. *AIP Conf. Proc.* **2016**, *1777*, 110005. [CrossRef]
30. Bravy, B.G.; Gordienko, V.M.; Platonenko, V.T. Kerr-assisted self-compression of mid-IR femtosecond laser pulse in dielectrics: Nonlinear medium choice. *J. Russ. Laser Res.* **2016**, *37*, 465–472. [CrossRef]
31. Pogorelsky, I.; Polyanskiy, M.; Babzien, M.; Palmer, M. Experiment on long-wave IR terawatt laser pulse compression to sub-picoseconds. In Proceedings of the OSA High-brightness Sources and Light-driven Interactions Congress, Washington, DC, USA, 16 November 2020. [CrossRef]
32. Polyanskiy, M.N.; Pogorelsky, I.V.; Babzien, M.; Vodopyanov, K.L.; Palmer, M.A. Nonlinear refraction and absorption properties of optical materials for high-peak-power long-wave-infrared lasers. *Opt. Mater. Express* **2024**, *14*, 696–714. [CrossRef]
33. Polyanskiy, M.N.; Pogorelsky, I.V.; Babzien, M.; Kupfer, R.; Vodopyanov, K.L.; Palmer, M.A. Post-compression of long-wave infrared 2 picosecond sub-terawatt pulses in bulk materials. *Opt. Express* **2021**, *29*, 31714–31725. [CrossRef] [PubMed]
34. Pogorelsky, I.V.; Polyanskiy, M.N.; Babzien, M.; Simmonds, A.; Palmer, M.A. Terawatt-class femtosecond long-wave infrared laser. *Front. Phys.* **2024**, *12*, 1390225. [CrossRef]

35. von Bergmann, H. High pressure CO_2 amplifiers for picosecond pulse amplification. *Proc. SPIE Int. Soc. Opt. Eng.* **2019**, *11042*, 110420N. [CrossRef]
36. Pogorelsky, I.V.; Polyanskiy, M.N.; Shaftan, T. Converting conventional electron accelerators to high peak brilliance Compton light sources. *Phys. Rev. Accel. Beams* **2020**, *23*, 120702. [CrossRef]
37. Chang, T.Y.; Wood, O.R. Optically pumped 33-atm CO_2 laser. *Appl. Phys. Lett.* **1973**, *23*, 370–373. [CrossRef]
38. Stenersen, K.; Wang, G. Direct optical pumping of high-pressure CO_2 and N_2O lasers with a pulsed HF pump laser. *IEEE J. Quant. Electron.* **1986**, *22*, 2236–2241. [CrossRef]
39. Martyshkin, D.; Karki, K.; Fedorov, V.; Mirov, S. Room temperature, nanosecond, 60 mJ/pulse Fe:ZnSe master oscillator power amplifier system operating at 3.8–5.0 μm. *Opt. Express* **2021**, *29*, 2387–2393. [CrossRef] [PubMed]
40. Tochitsky, S.; Tovey, D.; Pigeon, J.J.; Pogorelsky, I.V.; Joshi, C.; Polyanskiy, M.; Mirov, S.B. Status and prospects of optically pumped high-pressure CO_2 amplifiers. In Proceedings of the Advanced Accelerator Concepts Workshop, Long Island, NY, USA, 6 November 2022.
41. Keldysh, L. Ionization in the field of strong electromagnetic wave. *Sov. Phys. JETP* **1964**, *20*, 1307–1314. [CrossRef]
42. Woodbury, D.; Goffin, A.; Schwartz, R.M.; Isaacs, J.; Milchberg, H.M. Self-guiding of long-wave infrared laser pulses mediated by avalanche ionization. *Phys. Rev. Lett.* **2020**, *125*, 133201. [CrossRef] [PubMed]
43. Sprangle, P.; Tang, C.M.; Esarey, E. Relativistic self-focusing of short-pulse radiation beams in plasmas. *IEEE Trans. Plasma Sci.* **1987**, *15*, 145–153. [CrossRef]
44. Durfee, C.G., III; Milchberg, H.M. Light pipe for high intensity laser pulses. *Phys. Rev. Lett.* **1993**, *71*, 2409–2412. [CrossRef]
45. Kaganovich, D.; Sasorov, P.; Cohen, C.; Zigler, A. Variable profile capillary discharge for improved phase matching in a laser wakefield accelerator. *Appl. Phys. Lett.* **1999**, *75*, 772–774. [CrossRef]
46. Spence, D.J.; Hooker, S.M. Investigation of a hydrogen plasma waveguide. *Phys. Rev. E* **2000**, *63*, 015401. [CrossRef] [PubMed]
47. Miao, B.; Rockafellow, E.; Shrock, J.E.; Hancock, S.W.; Gordon, D.; Milchberg, H.M. Benchmarking of hydrodynamic plasma channels for multi-GeV laser-driven electron acceleration. *Phys. Rev. Accel. Beams* **2024**, *27*, 081302. [CrossRef]
48. Pogorelsky, I.V.; Pavlishin, I.V.; Ben-Zvi, I.; Kumita, T.; Kamiya, Y.; Hirose, T.; Greenberg, B.; Kaganovich, D.; Zigler, A.; Andreev, N.; et al. Transmission of high-power CO_2 laser pulses through a plasma channel. *Appl. Phys. Lett.* **2003**, *83*, 3459–3461. [CrossRef]
49. Dawson, J.M. Nonlinear electron oscillations in a cold plasma. *Phys. Rev.* **1959**, *113*, 383–387. [CrossRef]
50. Esarey, E.; Shadwick, B.A.; Schroeder, C.B.; Leemans, W.P. Nonlinear Pump Depletion and Electron Dephasing in Laser Wakefield Accelerators. In Proceedings of the Advanced Accelerator Concepts Workshop, AIP, New York, NY, USA, 21–26 June 2004; Volume 737, pp. 578–584. [CrossRef]
51. Frost, L.S.; Phelps, A.V. Rotational excitation and momentum transfer cross sections for electrons in H_2 and N_2 from transport coefficients. *Phys. Rev.* **1962**, *127*, 1621–1633. [CrossRef]
52. Engelhardt, A.G.; Phelps, A.V. Elastic and inelastic collision cross sections in hydrogen and deuterium from transport coefficients. *Phys. Rev.* **1963**, *131*, 2115–2118. [CrossRef]
53. Esarey, E.; Schroeder, C.B.; Leemans, W.P. Physics of laser-driven plasma-based electron accelerators. *Rev. Mod. Phys.* **2009**, *81*, 1229. [CrossRef]
54. Esarey, E.; Sprangle, P.; Krall, J.; Ting, A. Overview of plasma-based accelerator concepts. *IEEE Trans. Plasma Sci.* **1996**, *24*, 252–288. [CrossRef]
55. Tajima, T.; Dawson, J.M. Laser electron accelerator. *Phys. Rev. Lett.* **1979**, *43*, 267–270. [CrossRef]
56. Akhiezer, A.I.; Polovin, R.V. Theory of wave motion of an electron plasma. *Zhurnal Eksperimental Teor. Fiz.* **1956**, *30*, 915–928, *Sov. Phys. JETP* **1956**, *3*, 696–705.
57. Andreev, N.E.; Gorbunov, L.M.; Kirsanov, V.I.; Pogosova, A.A.; Ramazashvili, R.R. Resonant excitation of wakefields by a laser pulse in a plasma. *JETP Lett.* **1992**, *55*, 571–576.
58. Krall, J.; Ting, A.; Esarey, E.; Sprangle, P. Enhanced acceleration in a self-modulated-laser wake-field accelerator. *Phys. Rev. E* **1993**, *48*, 2157–2161. [CrossRef] [PubMed]
59. Pukhov, A.; Meyer-ter-Vehn, J. Laser wake field acceleration: The highly non-linear broken-wave regime. *Appl. Phys. B* **2002**, *74*, 355–361. [CrossRef]
60. Horton, A.; Tajima, T. Pump depletion in the plasma-beat-wave accelerator. *Phys. Rev. A* **1986**, *34*, 4110. [CrossRef] [PubMed]
61. King, P.M.; Miller, K.; Lemos, N.; Shaw, J.L.; Kraus, B.F.; Thibodeau, M.; Hegelich, B.M.; Hinojosa, J.; Michel, P.; Joshi, C.; et al. Predominant contribution of direct laser acceleration to high-energy electron spectra in a low-density self-modulated laser wakefield accelerator. *Phys. Rev. Accel. Beams* **2021**, *24*, 011302. [CrossRef]
62. Andreev, N.E.; Kuznetsov, S.V.; Pogosova, A.A.; Steinhauer, L.C.; Kimura, W.D. Modeling of laser wakefield acceleration at CO_2 laser wavelengths. *Phys. Rev. ST Accel. Beams* **2003**, *6*, 041301. [CrossRef]
63. Kumar, P.; Yu, K.; Rafal, Z.; Amorim, L.D.; Downer, M.C.; Welch, J.; Litvinenko, V.N.; Vafaei-Najafabadi, N.; Samulyak, R. Simulation study of CO_2 laser-plasma interactions and self-modulated wakefield acceleration. *Phys. Plasmas* **2019**, *26*, 083106. [CrossRef]

64. Zgadzaj, R.; Welch, J.; Cao, Y.; Amorim, L.D.; Cheng, A.; Gaikwad, A.; Iapozzutto, P.; Kumar, P.; Litvinenko, V.N.; Petrushina, I.; et al. Plasma electron acceleration driven by a long-wave-infrared laser. *Nat. Commun.* **2024**, *15*, 4037. [CrossRef] [PubMed]
65. Malka, V.; Fritzler, S.; Lefebvre, E.; Aleonard, M.-M.; Burgy, F.; Chambaret, J.-P.; Chemin, J.-F.; Krushelnick, K.; Malka, G.; Mangles, S.P.D.; et al. Electron acceleration by a wake field forced by an intense ultrashort laser pulse. *Science* **2002**, *298*, 1596–1600. [CrossRef]
66. Woodbury, D.; Feder, L.; Shumakova, V.; Gollner, C.; Schwartz, R.; Miao, B.; Salehi, F.; Korolov, A.; Pugžlys, A.; Baltuška, A.; et al. Laser wake field acceleration with mid-IR laser pulses. *Opt. Lett.* **2018**, *43*, 1131–1134. [CrossRef] [PubMed]
67. Gaikwad, A.S.; Petrushina, I.; Pogorelsky, I.V.; Kusche, K.; Li, W.; Miller, K.G.; Trommer, E.; Romasky, B.; Petrusky, M.E.; Petrusky, M.E.; et al. Field mapping of CO2-laser-driven LWFA at low density using electron beam probing. In Proceedings of the the 66th Annual Meeting of the APS Division of Plasma Physics, Atlanta, Georgia, 7–11 October 2024.
68. Gonsalves, A.J.; Nakamura, K.; Daniels, J.; Benedetti, C.; Pieronek, C.; de Raadt, T.C.H.; Steinke, S.; Bin, J.H.; Bulanov, S.S.; van Tilborg, J.; et al. Petawatt laser guiding and electron beam acceleration to 8 GeV in a laser-heated capillary discharge waveguide. *Phys. Rev. Lett.* **2019**, *122*, 084801. [CrossRef] [PubMed]
69. Aniculaesei, C.; Ha, T.; Yoffe, S.; Labun, L.; Milton, S.; McCary, E.; Spinks, M.M.; Quevedo, H.J.; Labun, O.Z.; Sain, R.; et al. The acceleration of a high-charge electron bunch to 10 GeV in a 10-cm nanoparticle-assisted wakefield accelerator. *Matter Radiat. Extrem.* **2024**, *9*, 014001. [CrossRef]
70. *2023 P5 Report: Exploring the Quantum Universe | Pathways to Innovation and Discovery in Particle Physics*; High Energy Physics Advisory Panel (HEPAP), US Department of Energy: Washington, DC, USA, 2023.
71. Schroeder, C.B.; Esarey, E.; Geddes, C.G.R.; Benedetti, C.; Leemans, W.P. Physics considerations for laser plasma linear colliders. *Phys. Rev. ST Accel. Beams* **2010**, *13*, 101301. [CrossRef]
72. Schroeder, C.B.; Albert, F.; Benedetti, C.; Bromage, J.; Bruhwiler, D.; Bulanov, S.; Campbell, E.; Cook, N.; Cros, B.; Downer, M.; et al. Linear colliders based on laser-plasma accelerators. *JINST* **2023**, *18*, T06001. [CrossRef]
73. Schroeder, C.B.; Esarey, E.; Leemans, W.P. Beamstrahlung considerations in laser-plasma-accelerator-based linear colliders. *Phys. Rev. ST Accel. Beams* **2012**, *15*, 051301. [CrossRef]
74. Downer, M.C. (The University of Texas, Austin, TX, USA). Personal communication, 2024.
75. Xu, X.L.; Wu, Y.P.; Zhang, C.J.; Li, F.; Wan, Y.; Hua, J.F.; Pai, C.-H.; Lu, W. Low emittance electron beam generation from a laser wakefield accelerator using two laser pulses with different wavelengths. *Phys. Rev. ST Accel. Beams* **2014**, *17*, 061301. [CrossRef]
76. Schroeder, C.B.; Vay, J.-L.; Esarey, E.; Bulanov, S.S.; Benedetti, C.; Yu, L.-L.; Chen, M.; Geddes, C.G.R.; Leemans, W.P. Thermal emittance from ionization-induced trapping in plasma accelerators. *Phys. Rev. ST Accel. Beams* **2014**, *17*, 101301. [CrossRef]
77. Wang, W.; Feng, K.; Ke, L.; Yu, C.; Xu, Y.; Qi, R.; Chen, Y.; Qin, Z.; Zhang, Z.; Fang, M.; et al. Free-electron lasing at 27 nanometers based on a laser wakefield accelerator. *Nature* **2021**, *595*, 516–520. [CrossRef]
78. Fuchs, J.; Antici, P.; d'Humieres, E.; Lefebvre, E.; Borghesi, M.; Brambrink, E.; Cecchetti, C.A.; Kaluza, M.; Malka, V.; Manclossi, M.; et al. Laser-driven proton scaling laws and new paths towards energy increase. *Nat. Phys.* **2006**, *2*, 48. [CrossRef]
79. Wilks, S.C.; Langdon, A.B.; Cowan, T.E.; Roth, M.; Singh, M.; Hatchett, S.; Key, M.H.; Pennington, D.; MacKinnon, A.; Snavely, R.A. Energetic proton generation in ultra-intense laser solid interactions. *Phys. Plasmas* **2001**, *8*, 542. [CrossRef]
80. Pogorelsky, I.V.; Yakimenko, V.; Polyanskiy, M.; Shkolnikov, P.; Ispiryan, M.; Neely, D.; McKenna, P.; Carroll, D.; Najmudin, Z.; Willingale, L. Ultrafast CO_2 laser technology: Application in ion acceleration. *Nucl. Instrum. Meth. Phys. Res. A* **2010**, *620*, 67–70. [CrossRef]
81. Park, J.; Bin, J.H.; Steinke, S.; Ji, Q.; Bulanov, S.S.; Thévenet, M.; Vay, J.-L.; Schenkel, T.; Geddes, C.G.R.; Schroeder, C.B.; et al. Target normal sheath acceleration with a large laser focal diameter. *Phys. Plasmas* **2020**, *27*, 123104. [CrossRef]
82. Robinson, A.P.L.; Zepf, M.; Kar, S.; Evans, R.G.; Bellei, C. Radiation pressure acceleration of thin foils with circularly polarized laser pulses. *New J. Phys.* **2008**, *10*, 013021. [CrossRef]
83. Macchi, A. Theory of light sail acceleration by intense lasers: An overview. *High Power Laser Sci. Eng.* **2014**, *2*, e10. [CrossRef]
84. Robinson, A.P.L.; Gibbon, P.; Zepf, M.; Kar, S.; Evans, R.G.; Bellei, C. Relativistically correct hole-boring and ion acceleration by circularly polarized laser pulses. *Plasma Phys. Contr. Fusion* **2009**, *51*, 024004. [CrossRef]
85. Schlegel, T.; Naumova, N.; Tikhonchuk, V.T.; Labaune, C.; Sokolov, I.V.; Mourou, G. Relativistic laser piston model: Ponderomotive ion acceleration in dense plasmas using ultraintense laser pulses. *Phys. Plasmas* **2009**, *16*, 083103. [CrossRef]
86. Moiseev, S.S.; Sagdeev, R.Z. Collisionless shock waves in a plasma in a weak magnetic field. *J. Nucl. Energy C* **1963**, *51*, 43–47. [CrossRef]
87. Fiuza, F.; Fonseca, R.; Tonge, J.; Mori, W.; Silva, L. Weibel-instability-mediated collisionless shocks in the laboratory with ultraintense lasers. *Phys. Rev. Lett.* **2012**, *108*, 235004. [CrossRef]
88. Haberberger, D.; Tochitsky, S.; Fiuza, F.; Gong, C.; Fonseca, R.A.; Silva, L.O.; Mori, W.B.; Joshi, C. Collisionless shocks in laser produced plasma generate monoenergetic high-energy proton beams. *Nat. Phys.* **2011**, *8*, 95–99. [CrossRef]

89. Palmer, C.A.J.; Dover, N.P.; Pogorelsky, I.; Babzien, M.; Dudnikova, G.I.; Ispiriyan, M.; Polyanskiy, M.N.; Schreiber, J.; Shkolnikov, P.; Yakimenko, V.; et al. Monoenergetic proton beams accelerated by a radiation pressure driven shock. *Phys. Rev. Lett.* **2011**, *106*, 014801. [CrossRef] [PubMed]
90. Palmer, C.A.J.; Dover, N.P.; Pogorelsky, I.; Streeter, M.J.V.; Najmudin, Z. Manipulation of laser-generated energetic proton spectra in near critical density plasma. *J. Plasma Phys.* **2015**, *81*, 365810103. [CrossRef]
91. Dover, N.P.; Cook, N.; Tresca, O.; Ettlinger, O.C.; Maharjan, C.; Polyanskiy, M.N.; Shkolnikov, P.; Pogorelsky, I.; Najmudin, Z. Optical shaping of gas targets for laser-plasma ion sources. *J. Plasma Phys.* **2016**, *82*, 415820101. [CrossRef]
92. Chen, Y.-H.; Ting, A.; Hafizi, B.; Helle, M.H.; Johnson, L.A.; Polyanskiy, M.N.; Pogorelsky, I.V.; Babzien, M.; Dover, N.P.; Ettlinger, O.C.; et al. Proton acceleration in an overdense hydrogen plasma by intense CO_2 laser pulses with nonlinear propagation effects in the underdense pre-plasma. *Phys. Plasmas* **2023**, *30*, 053106. [CrossRef]
93. Savert, A.; Mangles, S.P.D.; Schnell, M.; Siminos, E.; Cole, J.M.; Leier, M.; Reuter, M.; Schwab, M.B.; Möller, M.; Poder, K.; et al. Direct observation of the injection dynamics of a laser wakefield accelerator using few-femtosecond shadowgraphy. *Phys. Rev. Lett.* **2015**, *115*, 055002. [CrossRef]
94. Ettlinger, O.C. Studies of Near-Critical Density Laser Plasma Interactions for Ion Acceleration. PhD Thesis, Imperial College London, London, UK, 12 January 2018.
95. Dover, N.P.; Tresca, O.; Cook, N.; Ettlinger, O.C.; Kingham, R.J.; Maharjan, C.; Polyanskiy, M.N.; Shkolnikov, P.; Pogorelsky, I.; Najmudin, Z. Optical imaging of laser-driven fast electron Weibel-like filamentation in overcritical density plasma. *Phys. Rev. Lett.* **2025**, *134*, 025102. [CrossRef]
96. Bakshi, V. (Ed.) *EUV Lithography*; SPIE: Bellingham, WA, USA, 2009.
97. Ueno, Y.; Ariga, T.; Soumagne, G.; Higashiguchi, T.; Kubodera, S.; Pogorelsky, I.; Pavlishin, I.; Stolyarov, D.; Babzien, M.; Kusche, K.; et al. Efficient extreme ultraviolet plasma source generated by a CO_2 laser and a liquid xenon microjet target. *Appl. Phys. Lett.* **2007**, *90*, 191503. [CrossRef]
98. Microsoft Word—Laser Technology Workshop Report_20240117_Update. Available online: https://science.osti.gov/-/media/ardap/pdf/2024/Laser-Technology-Workshop-Report_20240105_final.pdf (accessed on 10 February 2024).
99. Lewenstein, M.; Balcou, P.; Ivanov, M.Y.; L'Huillier, A.; Corkum, P.B. Theory of high-harmonic generation by low-frequency laser fields. *Phys. Rev. A* **1994**, *49*, 2117–2132. [CrossRef]
100. Krause, J.L.; Schafer, K.J.; Kulander, K.C. High-order harmonic generation from atoms and ions in the high intensity regime. *Phys. Rev. Lett.* **1992**, *68*, 3535–3538. [CrossRef] [PubMed]
101. Fu, Y.; Nishimura, K.; Shao, R.; Suda, A.; Midorikawa, K.; Lan, P.; Takahashi, E.J. High efficiency ultrafast water-window harmonic generation for single-shot soft X-ray spectroscopy. *Commun. Phys.* **2020**, *3*, 92. [CrossRef]
102. Tate, J.; Auguste, T.; Muller, H.G.; Salieres, P.; Agostini, P.; DiMauro, L.F. Scaling of Wave-Packet Dynamics in an Intense Midinfrared Field. *Phys. Rev. Lett.* **2007**, *98*, 013901. [CrossRef] [PubMed]
103. Popmintchev, T.; Chen, M.-C.; Popmintchev, D.; Arpin, P.; Brown, S.; Alisauskas, S.; Andriukaitis, G.; Balčiunas, T.; Mücke, O.D.; Pugzlys, A.; et al. Bright coherent ultrahigh harmonics in the keV x-ray regime from mid-infrared femtosecond lasers. *Science* **2012**, *336*, 1287–1291. [CrossRef]
104. Li, X.; Qiu, T.; Zhang, J.; Baldini, E.; Lu, J.; Rappe, A.M.; Nelson, K.A. Terahertz field-induced ferroelectricity in quantum paraelectric $SrTiO_3$. *Science* **2019**, *364*, 1079. [CrossRef]
105. Nanni, E.A.; Huang, W.R.; Hong, K.-H.; Ravi, K.; Fallahi, A.; Moriena, G.; Dwayne Miller, R.J.; Kärtner, F.X. Terahertz driven linear electron acceleration. *Nat. Commun.* **2015**, *6*, 8486. [CrossRef]
106. Pickwell, E.; Wallace, V.P. Biomedical applications of terahertz technology. *J. Phys. D* **2006**, *39*, R301. [CrossRef]
107. Fitzgerald, A.J.; Berry, E.; Zinov'ev, N.N.; Homer-Vanniasinkam, S.; Miles, R.E.; Chamberlain, J.M.; Smith, M.A. Catalogue of human tissue optical properties at terahertz frequencies. *J. Biol. Phys.* **2003**, *29*, 123–128. [CrossRef]
108. Casalbuoni, S.; Schmidt, B.; Schmüser, P.; Arsov, V.; Wesch, S. Ultrabroadband terahertz source and beamline based on coherent transition radiation. *Phys. Rev. ST Accel. Beams* **2009**, *12*, 030705. [CrossRef]
109. Fülöp, J.A.; Polónyi Gy Monoszlai, B.; Andriukaitis, G.; Balciunas, T.; Pugzlys, A.; Arthur, G.; Baltuska, A.; Hebling, J. Highly efficient scalable monolithic semiconductor terahertz pulse source. *Optica* **2016**, *3*, 1075–1078. [CrossRef]
110. Krasilnikov, M.; Aboulbanine, Z.; Adhikari, G.; Aftab, N.; Asoyan, A.; Boonpornprasert, P.; Davtyan, H.; Georgiev, G.; Good, J.; Grebinyk, A.; et al. First high peak and average power single-pass THz FEL based on high brightness photoinjector. *arXiv* **2024**, arXiv:2405.19152.
111. Tóth, G.; Illés, G.; Nazymbekov, G.; Mbithi, N.; Almási, G.; Hebling, J. Possibility of CO_2 laser-pumped multi-millijoule-level ultrafast pulse terahertz sources. *Sci. Rep.* **2024**, *14*, 999. [CrossRef]
112. Liao, G.-Q.; Liu, H.; Scott, G.G.; Zhang, Y.-H.; Zhu, B.-J.; Zhang, Z.; Li, Y.T.; Armstrong, C.; Zemaityte, E.; Bradford, P.; et al. Towards terawatt-scale spectrally tunable terahertz pulses via relativistic laser-foil interactions. *Phys. Rev. X* **2020**, *10*, 031062. [CrossRef]

113. Petrillo, V.; Bacci, A.; Zinati, R.B.A.; Chaikovska, I.; Curatolo, C.; Ferrario, M.; Maroli, C.; Ronsivalle, C.; Rossi, A.; Serafini, L.; et al. Photon flux and spectrum of gamma-ray sources. *Nucl. Instrum. Methods Phys. Res. A* **2012**, *693*, 109–116. [CrossRef]
114. Pogorelsky, I.V.; Ben-Zvi, I.; Hirose, T.; Kashiwagi, S.; Yakimenko, V.; Kusche, K.; Siddons, P.; Skaritka, J.; Kumita, T.; Tsunemi, A.; et al. Demonstration of 8×10^{18} photons/second peaked at 1.8 Å in a relativistic Thomson scattering experiment. *Phys. Rev. ST Accel. Beams* **2000**, *3*, 090702. [CrossRef]
115. Endrizzi, M.; Gureyev, T.E.; Delogu, P.; Oliva, P.; Golosio, B.; Carpinelli, M.; Pogorelsky, I.; Yakimenko, V.; Bottigli, U. Quantitative phase retrieval with picosecond x-ray pulses from the ATF Inverse Compton Scattering source. *Opt. Express* **2011**, *19*, 2748–2753. [CrossRef] [PubMed]
116. Oliva, P.; Carpinelli, M.; Golosio, B.; Delogu, P.; Endrizzi, M.; Park, J.; Pogorelsky, I.; Yakimenko, V.; Williams, O.; Rosenzweig, J. Quantitative evaluation of single-shot inline phase contrast imaging using an inverse Compton X-ray source. *Appl. Phys. Lett.* **2010**, *97*, 134104. [CrossRef]
117. Babzien, B.; Ben-Zvi, I.; Kusche, K.; Pavlishin, I.V.; Pogorelsky, I.V.; Siddons, D.P.; Yakimenko, V.; Cline, D.; Zhou, F.; Hirose, T.; et al. Observation of the second harmonic in Thomson scattering from relativistic electrons. *Phys. Rev. Lett.* **2006**, *96*, 054802. [CrossRef] [PubMed]
118. Sakai, Y.; Pogorelsky, I.; Williams, O.; O'Shea, F.; Barber, S.; Gadjev, I.; Duris, J.; Musumeci, P.; Fedurin, M.; Korostyshevsky, A.; et al. Observation of redshifting and harmonic radiation in inverse Compton scattering. *Phys. Rev. STAB* **2015**, *18*, 060702. [CrossRef]
119. Krafft, G.; Priebe, G. Compton sources of electromagnetic radiation. *Rev. Accel. Sci. Techol.* **2010**, *3*, 147. [CrossRef]
120. Feser, M. The Lyncean Compact Light Source: X-ray synchrotron radiation for analytical and imaging applications (Conference Presentation). In Proceedings of the SPIE Optical Engineering + Applications, San Diego, CA, USA, 19 September 2017; Volume 10387, p. 1038703. [CrossRef]
121. Akagi, T.; Kosuge, A.; Araki, S.; Hajima, R.; Honda, Y.; Miyajima, T.; Mori, M.; Nagai, R.; Nakamura, N.; Shimada, M.; et al. Narrow-band photon beam via laser Compton scattering in an energy recovery linac. *Phys. Rev. Accel. Beams* **2016**, *19*, 114701. [CrossRef]
122. Zamfir, V.; Tanaka, K.; Ur, C. Extreme Light Infrastructure—Nuclear Physics (ELI-NP). *Europhys. News* **2019**, *50*, 23–25. [CrossRef]
123. Deitrick, K.E.; Franck, C.; Hofstaetter, G.H.; Kostroun, V.O.; Smolenski, K.W.; Crone, J.; Owen, H.L.; Muratori, B.D. A hard x-ray compact Compton source at CBETA. In Proceedings of the IPAC2019, Melbourne, Australia, 19–24 May 2019. [CrossRef]
124. Alesini, D.; Chaikovska, I.; Guiducci, S.; Milardi, C.; Variola, A.; Zobov, M.; Zomer, F. DAΦNE γ-rays factory. *IEEE Trans. Nucl. Sci.* **2016**, *63*, 913–920. [CrossRef]
125. Hirose, T.; Dobashi, K.; Kurihara, Y.; Muto, T.; Omori, T.; Okugi, T.; Sakai, I.; Urakawa, J.; Washio, M. Polarized positron source for the linear collider, JLC. *Nucl. Instrum. Methods Phys. Res. A* **2000**, *455*, 15. [CrossRef]
126. Yakimenko, V.; Pogorelsky, I.V. Polarized γ source based on Compton backscattering in a laser cavity. *Phys. Rev. STAB* **2006**, *9*, 091001. [CrossRef]
127. Shen, Y.R. *The Principles of Nonlinear Optics*; John Wiley & Sons: Hoboken, NJ, USA, 1984; Chapter 17.
128. Durand, M.; Houard, A.; Prade, B.; Mysyrowicz, A.; Durecu, A.; Moreau, B.; Fleury, D.; Vasseur, O.; Borchert, H.; Diener, K.; et al. Kilometer range filamentation. *Opt. Express* **2013**, *21*, 26836–26845. [CrossRef]
129. Mechain, G.; Couairon, A.; André, Y.-B.; D'Amico, C.; Franco, M.; Prade, B.; Tzortzakis, S.; Mysyrowicz, A.; Sauerbrey, R. Long range self-channeling of infrared laser pulses in air: A new propagation regime without ionization. *App. Phys. B* **2004**, *79*, 379–382. [CrossRef]
130. Tochitsky, S.Y.; Welch, E.C.; Matteo, D.A.; Panagiotopoulos, P.; Kolesik, M.; Moloney, J.V.; Joshi, C. Self-channeling of a multi-Joule 10 μm picosecond pulse train through long distances in air. *Opt. Express* **2024**, *32*, 2067–2080. [CrossRef] [PubMed]
131. Tochitsky, S.; Welch, E.; Polyanskiy, M.; Pogorelsky, I.; Panagiotopoulos, P.; Kolesik, M.; Wright, E.M.; Koch, S.W.; Moloney, J.V.; Pigeon, J.; et al. Megafilament in air formed by self-guided terawatt long-wavelength infrared laser. *Nat. Photon.* **2019**, *13*, 41–46. [CrossRef]
132. Tochitsky, S.; Welch, E.; Panagiotopoulos, P.; Polyanskiy, M.; Pogorelsky, I.; Kolesik, M.; Koch, S.W.; Moloney, J.V.; Joshi, C. Filamentation of long-wave infrared pulses in the atmosphere. *JOSA B* **2019**, *36*, G40–G51. [CrossRef]
133. Isaacs, J.; Miao, C.; Sprangle, P. Remote monostatic detection of radioactive material by laser-induced breakdown. *Phys. Plasmas* **2016**, *23*, 033507. [CrossRef]
134. Zingale, A.; Waczynski, S.; Pogorelsky, I.; Polyanskiy, M.; Sears, J.; Lakis, R.E.; Milchberg, H.M. Remote detection of radioactive material using a short pulse CO_2 laser. *arXiv* **2024**, arXiv:2408.13640. [CrossRef]
135. Zingale, A.; Waczynski, S.; Sears, J.; Lakis, R.E.; Milchberg, H.M. Atmospheric effects on the laser-driven avalanche-based remote detection of radiation. *Opt. Lett.* **2023**, *48*, 2480. [CrossRef] [PubMed]
136. Englesbe, A.; Elle, J.; Schwartz, R.; Garrett, T.; Woodbury, D.; Jang, D.; Kim, K.-Y.; Milchberg, H.; Reid, R.; Lucero, A.; et al. Ultrabroadband microwave radiation from near- and mid-infrared laser-produced plasmas in air. *Phys. Rev. A* **2021**, *104*, 013107. [CrossRef]

137. Thornton, E.A. Optimizing Ultra-Broadband Microwave Radiation Through Plasma Dynamics of USPL Filaments. Ph.D. Thesis, University of North Texas, Denton, TX, USA, July 2024.
138. Kimura, W.D.; Kim, G.H.; Romea, R.D.; Steinhauer, L.C.; Pogorelsky, I.V.; Kusche, K.P.; Fernow, R.C.; Wang, X.; Liu, Y. Laser acceleration of relativistic electrons using the inverse Cherenkov effect. *Phys. Rev. Lett.* **1995**, *74*, 546–549. [CrossRef]
139. Li, W.H.; Pogorelsky, I.V.; Palmer, M.A. Direct Acceleration of an electron beam with a radially polarized long-wave infrared laser. *Photonics* **2024**, *11*, 1066. [CrossRef]
140. Jana, K.; Mi, Y.; Møller, S.H.; Ko, D.H.; Gholam-Mirzaei, S.; Abdollahpour, D.; Sederberg, S.; Corkum, P.B. Quantum control of flying doughnut terahertz pulses. *Sci. Adv.* **2024**, *10*, eadl1803. [CrossRef] [PubMed]
141. Kimura, W.D.; Campbell, L.P.; Dilley, C.E.; Gottschalk, S.C.; Quimby, D.C.; van Steenbergen, A.; Babzien, M.; Ben-Zvi, I.; Gallardo, J.C.; Kusche, K.P.; et al. Detailed experimental results for laser acceleration staging. *Phys. Rev. ST Accel. Beams* **2001**, *4*, 101301. [CrossRef]
142. Yu, L.-H.; Babzien, M.; Ben-Zvi, I.; DiMauro, L.F.; Doyuran, A.; Graves, W.; Johnson, E.; Babzien, M.; Ben-Zvi, I.; Gallardo, J.C.; et al. High-gain harmonic-generation free-electron laser. *Science* **2000**, *289*, 932–934. [CrossRef] [PubMed]
143. Duris, J.; Musumeci, P.; Babzien, M.; Fedurin, M.; Kusche, K.; Li, R.K.; Moody, J.; Pogorelsky, I.; Polyanskiy, M.; Rosenzweig, J.B.; et al. High-quality electron beams from a helical inverse free-electron laser accelerator. *Nat. Commun.* **2014**, *5*, 4928. [CrossRef] [PubMed]
144. Ovodenko, A.; Agustsson, R.; Babzien, M.; Campese, T.; Fedurin, M.; Murokh, A.; Pogorelsky, I.; Polyanskiy, M.; Rosenzweig, J.; Sakai, Y.; et al. High duty cycle inverse Compton scattering x-ray source. *Appl. Phys. Lett.* **2016**, *109*, 253504. [CrossRef]
145. Gadjev, I.; Sudar, N.; Babzien, M.; Duris, J.; Hoang, P.; Fedurin, M.; Kusche, K.; Malone, R.; Musumeci, P.; Palmer, M.; et al. An inverse free electron laser acceleration-driven Compton scattering X-ray source. *Sci. Rep.* **2019**, *9*, 532. [CrossRef] [PubMed]